Non-canonical, potassium-driven cerebrospinal fluid clearance

Huixin Xu[1,‡], Ryann M Fame[1,‡], Cameron Sadegh[1,2], Jason Sutin[3], Christopher Naranjo[4], Della Syau[4], Jin Cui[1], Frederick B Shipley[1,5], Amanda Vernon[6], Fan Gao[6,†], Yong Zhang[7], Michael J. Holtzman[7], Myriam Heiman[6], Benjamin C Warf[8], Pei-Yi Lin[3], Maria K Lehtinen[1,5 *]

[1]Department of Pathology, Boston Children's Hospital, Boston, MA 02115, USA

[2]Department of Neurosurgery, Massachusetts General Hospital and Harvard Medical School, Boston, MA 02114, USA

[3]Fetal-Neonatal Neuroimaging and Developmental Science Center, Division of Newborn Medicine, Boston Children's Hospital, Harvard Medical School, 300 Longwood Avenue, Boston, MA 02115, USA

[4]Summer Honors Undergraduate Research Program, Division of Medical Sciences, Harvard Medical School, Boston, MA 02115, USA

[5]Graduate Program in Biophysics, Harvard University, Cambridge, MA 02138, USA

[6]Broad Institute of MIT and Harvard, Cambridge, MA 02142; Picower Institute for Learning and Memory, Cambridge, MA 02139; Department of Brain and Cognitive Sciences, Massachusetts Institute of Technology, Cambridge, MA 02139, USA

[7]Pulmonary and Critical Care Medicine, Department of Medicine, Washington University, St. Louis, MO 63110, USA

[8]Department of Neurosurgery, Boston Children's Hospital, Boston, MA 02115, USA

[‡]These authors contributed equally.

[†]Current address: Bioinformatics Resource Center in the Beckman Institute at Caltech, Pasadena, CA 91125, USA

*Correspondence should be addressed to: maria.lehtinen@childrens.harvard.edu

ABSTRACT

Cerebrospinal fluid (CSF) provides vital support for the brain. Abnormal CSF accumulation is deleterious for perinatal neurodevelopment, but how CSF leaves the brain during this critical period is unknown. We found in mice a postnatal neurodevelopmental transition phase featuring precipitous CSF K^+ clearance, accompanied by water, through the choroid plexus (ChP). The period corresponds to a human fetal stage when canonical CSF clearance pathways have yet to form and congenital hydrocephalus begins to manifest. Unbiased ChP metabolic and ribosomal profiling highlighted this transition phase with increased ATP yield and activated energy-dependent K^+ transporters, in particular the Na^+-K^+-Cl^- and water cotransporter NKCC1. ChP-targeted NKCC1 overexpression enhanced K^+-driven CSF clearance and enabled more permissive cerebral hydrodynamics. Moreover, ventriculomegaly in an obstructive hydrocephalus model was improved by ChP-targeted NKCC1 overexpression. Collectively, we identified K^+-driven CSF clearance through ChP during a transient but critical neurodevelopmental phase, with translational value for pathologic conditions.

Keywords: cerebrospinal fluid; clearance; potassium; choroid plexus; development; NKCC1; hydrocephalus

INTRODUCTION

A balance between cerebrospinal fluid (CSF) production and clearance (influx/efflux) is essential for normal brain function and development (Fame and Lehtinen, 2020). Disrupted CSF volume homeostasis with excessive CSF accumulation is implicated in many pediatric brain disorders, in particular congenital hydrocephalus (Kahle et al., 2016), where patients suffer from a potentially life-threatening accumulation of CSF and frequently develop neurological deficits that last through childhood and into adult life (Vinchon et al., 2012). Schizophrenia patients can have enlarged lateral ventricles by their first episode of psychosis (Steen et al., 2006), and in some cases as early as infancy (Gilmore et al., 2010), suggesting a role for CSF clearance abnormalities in this and possibly other neurodevelopmental disorders. As another example, autism spectrum disorders are associated with altered CSF distribution patterns and enlarged CSF space surrounding the brain (Shen et al., 2017). A better understanding of developing CSF dynamics may help explain why early phases of brain development (e.g. from third trimester to 6 months after birth in human) represent a period of high vulnerability to certain congenial disorders (Volpe, 2008, Gilmore et al., 2010, Shen et al., 2017).

Critically, how CSF is cleared during this perinatal period remains a mystery. Progress in CSF dynamics research has identified several CSF clearance routes including arachnoid granulations, perineural and paravascular pathways, and meningeal lymphatics (Antila et al., 2017, Munk et al., 2019, Fame and Lehtinen, 2020). However, these systems only fully appear at later stages of life (up to 2 years in human and several weeks postnatal in mice) (Antila et al., 2017, Munk et al., 2019), and therefore are not available to contribute to CSF dynamics during these critical early phases. Identifying and manipulating the early endogenous CSF clearance mechanisms could provide one powerful approach for tackling neurodevelopmental disorders

involving CSF dysregulation, and may also be applied to fluid disorders affecting adults.

To identify how early CSF is cleared, we investigated tissues with the ability to modulate CSF at this stage. The choroid plexus (ChP) is an intraventricular epithelial structure that forms the majority of the blood-CSF barrier and develops prenatally. It contains diverse ion and fluid transporters along its vast surface area capable of bidirectional transport (Damkier et al., 2013). Although the prevailing model posits that the ChP provides net unidirectional, luminal secretion of ions and water to form CSF, insufficient corroborating data have been collected under physiological experimental conditions. Furthermore, historical clinical observations suggest some absorptive functions of the ChP (Milhorat et al., 1970) which is supported by animal studies (Oreskovic et al., 2017). Finally, broad transcriptional changes of the machinery regulating fluid/ion transport support the concept of temporally dynamic and possibly context-dependent ChP functions in determining net directionality of CSF transport (Liddelow et al., 2013, Delpire and Gagnon, 2019).

To further explore potentially absorptive properties of the ChP, we studied the expression of transporters, the energetic systems and ionic gradients that govern their activity, and their physiological effects across the timespan of early postnatal development in mice. Taken together our data support a novel role and mechanism for CSF clearance by the Na^+-K^+-Cl^- and water co–transporter, NKCC1, in the apical membrane of the ChP during a specific developmental period. These results have implications for the pathophysiology of congenital disorders accompanied by dysregulated CSF and could inform strategies for treatment of neonatal hydrocephalus and perhaps other disorders.

RESULTS

CSF K^+ declines precipitously during a specific perinatal period

We discovered a unique and transient phase of neurodevelopment when CSF [K^+] decreased rapidly. We used inductively coupled plasma optical emission spectrometry (ICP-OES) and ion chromatography (IC) to measure levels of key ions likely to govern CSF flux including Na^+, K^+, and Cl^- at several developmental timepoints. CSF [K^+] was remarkably high at birth (9.6 ± 3.5 mM), decreased rapidly to 4.4 ± 0.9 mM by P7 (**Fig. 1A**), and later achieved adult levels of 3.1 ± 0.6 mM (**Fig. 1A**) while [Na^+] and [Cl^-] were minimally changed (**Fig. 1B**). The reduction in CSF K^+ was consistent with previous reports in other species (Saunders et al., 2018) and correlated with parallel changes in serum [K^+] such that the ratio between blood and CSF [K^+] remained stable (**Fig. 1C**).

Notably, K^+ transport has been associated with water co-transport by several K^+ transporters in various tissues and cell types (Zeuthen, 1994, Hamann et al., 2010, Zeuthen and Macaulay, 2012), suggesting that CSF [K^+] changes could drive water movement in the brain as well. Therefore, we sought to identify mechanisms underlying this fast clearance of CSF K^+, which may shed light on CSF outflow during this time.

ChP metabolism increases during the early postnatal transition phase

We found that the transitional period of rapid CSF K^+ clearance coincided with high ChP metabolism. We reasoned that K^+ clearance during this period could be ChP-mediated because the ChP expresses high levels of K^+ co-transporters on its large CSF-contacting surface area (Keep and Jones, 1990, Damkier et al., 2013). Similar to water and ion transport by other epithelial structures such as kidney proximal and distal tubes (Bhargava and Schnellmann, 2017),

113 K^+ clearance from CSF by the ChP would be energy-dependent and therefore be accompanied by
114 upregulation of ATP production and mitochondrial activity. Therefore, we evaluated the
115 metabolic status and ATP production capacity of the ChP epithelium before, during, and after the
116 time period of CSF [K^+] reduction. We found that both mitochondria number and size increased
117 from E16.5 to 2mo (**Fig. 1D-G**), while cellular glycogen load gradually decreased
118 (**Supplementary Fig. 1**). Both observations are consistent with reports from ChP in other
119 mammalian species (Netsky and Shuangshoti, 1975, Keep and Jones, 1990) and suggest
120 functional changes in ChP oxidative metabolism. To assess this we monitored oxygen
121 consumption to calculate basal metabolism and ATP production at embryonic day 16.5 (E16.5),
122 postnatal day 0 (P0), P7, and adult (2 months old (2mo)) ChP explants using Agilent Seahorse
123 XFe technology (**Fig. 1H, Supplementary Fig. 2**). We found that E16.5 ChP had the lowest
124 basal respiration of all tested ages (**Fig. 1I, Supplementary Fig. 2**). Adult had a higher capacity
125 for overall ATP production than E16.5 ChP, but surprisingly, P0-P7 ChP were the most
126 metabolically active as per ATP production (**Fig. 1I, J**). In addition, mitochondrial subcellular
127 distribution in ChP epithelium was biased toward the apical surface as postnatal development
128 proceeded, with E16.5 mitochondria heavily distributed along the basal side of epithelial cells,
129 P0 mitochondria intermediately localized, and P7 and 2mo mitochondria having more apical
130 distribution (**Fig. 1K-M, Supplementary Fig. 3**). Mitochondrial subcellular localization
131 responds to regional energy demand in other cellular processes such as migration of mouse
132 embryonic fibroblasts and during axonal outgrowth (Schuler et al., 2017, Smith and Gallo, 2018).
133 Together with the increase in ATP production postnatally, the shift in ChP epithelial
134 mitochondria distribution over postnatal development suggests increasing ATP supply to meet
135 high demand at the apical ChP surface during the early postnatal phase, concurrent with the rapid

clearance of CSF K^+. This concurrence prompted us to investigate energy-dependent mechanisms whereby ChP epithelial cells might contribute to K^+ clearance.

The ChP increases production of CSF-facing ion and water transporters postnatally

Consistent with rapid CSF K^+ clearance and high ChP metabolism, we found that expression of the energy-dependent cation transport pathway components were upregulated in ChP postnatally. To unbiasedly identify candidates controlling postnatal CSF clearance through the ChP, we conducted ribosomal profiling to investigate transcripts that are prioritized for translation in embryonic (E16.5) and adult (2 mo) ChP, using Translating Ribosomal Affinity Purification (TRAP; Heiman et al., 2008). ChP epithelial cells were targeted by crossing *FoxJ1:cre* mice (Zhang et al., 2007) with *TRAP* (*EGFP:L10a*) mice (Heiman et al., 2008) (**Fig. 2A, Supplementary Fig. 4A, B**), and mRNA associated with the L10a ribosomal subunit were purified for sequencing.

TRAP analyses revealed 1967 differentially translated transcripts (adjusted $p < 0.05$) between E16.5 and 2mo adult ChP: 1119 enriched at E16.5 and 847 enriched at 2mo (**Fig. 2B**). Gene set and pathway analyses revealed developmentally regulated ChP programs. Adult (2mo) ChP had enriched functional gene sets associated with active transmembrane membrane transport and mitochondria, which is consistent with our abovementioned findings on metabolism changes (**Fig. 2C**). Specifically, cation transport was enriched, supporting the hypothesis of ChP mediating CSF K^+ transport postnatally (**Fig. 2C, D**). Enriched pathways in the 2mo adult included secretion associated pathways named for other, better studied secretory processes, including salivary and pancreatic secretion, all of which have a special emphasis on water and ion transmembrane transport (**Supplementary Fig. 4C (red), D**). Consistent with a rise in fluid and ion modulating machinery, there was a striking enrichment of more

159 transmembrane and signal peptide-containing transcripts in adult ChP (**Supplementary Fig. 4E,**
160 **F**). These results indicate that the ChP specifically gained fluid and ion modulatory functions
161 postnatally.
162
163 **NKCC1 is poised to mediate perinatal ChP CSF K^+ and water clearance**
164 Among all fluid and ion modulating candidates with increasing postnatal expression
165 (**Supplementary Fig. 4G, H**), we identified NKCC1 (*Slc12a2*) as the candidate most likely to
166 mediate CSF clearance. NKCC1 is functionally related to Na^+/K^+-ATPase (*Atp1a1* and *Atp1b1*),
167 as the latter actively maintains the Na^+/K^+ gradient that powers NKCC1. Both Na^+/K^+-ATPase
168 and NKCC1 are capable of CSF K^+ clearance, but NKCC1 was of particular interest because (1)
169 it is a co-transporter of K^+ and water (Zeuthen and Macaulay, 2012, Steffensen et al., 2018); and
170 (2) the activity of NKCC1 can be further modified by phosphorylation (Darman and Forbush,
171 2002), lending additional control to its fluid/ion modulatory capacity. In addition, NKCC1 is
172 particularly enriched in the ChP and does not impact broad functionality like the Na^+/K^+-ATPase
173 does, both of which are ideal features for a functional therapeutic intervention target. We refined
174 our temporal expression analyses of NKCC1, ATP1a1, ATP1b1, and Klotho (*Kl*), which
175 contributes to the membrane localization of the Na^+/K^+-ATPase (Razzaque, 2008, Sopjani et al.,
176 2011) (**Fig. 2E**), by sampling weekly from P0 to P28 and then at 2mo and confirmed increased
177 expression of transcript and protein for each component across developmental time (**Fig. 2F, G,**
178 **Supplementary Fig. 5**). The observed changes in NKCC1 total protein were corroborated by an
179 independent approach where the rate of ChP epithelial cell swelling under high $[K^+]$ challenge
180 (Steffensen et al., 2018) reflected the abundance of NKCC1 protein (**Fig. 2H-J, Supplementary**
181 **Fig. 6**).

In addition, we found particularly high levels of phosphorylated, therefore activated (Darman and Forbush, 2002), NKCC1 (pNKCC1) in the ChP of P0-P7 pups, with P7 having peak pNKCC1 levels among all postnatal ages, indicative of increased NKCC1 activity during the first postnatal week (**Fig. 2G**). Similar to the timeline of ChP ATP production (**Fig. 1J**), the timeframe of high ChP pNKCC1 was concurrent with the fast CSF [K^+] decrease during the first postnatal week (**Fig. 1A**), suggesting a functional correlation and further confirming the significance of the early postnatal transitional period. Taken together, we identified ChP NKCC1 as the top candidate for mediating postnatal CSF K^+ and water clearance.

NKCC1 temporal regulation requires epigenetic control that is implicated in congenital hydrocephalus

We found that the temporal profile of NKCC1 expression was tightly regulated at the epigenetic level by modulators implicated in some forms of congenital hydrocephalus. The NuRD complex governs differentiation and maturation of diverse cells and tissues (Goodman and Bonni, 2019). Our previously published RNA sequencing studies (Lun et al., 2015) identified NuRD components, including the ATPase CHD family members (Chd4 being the most highly expressed), the histone deacetylases HDAC1/2, and methyl CpG-binding domain protein MBD3 in the ChP (**Fig. 3A**). *De novo* loss-of-function CHD4 mutations are implicated in some groups of children with congenital hydrocephalus and ventriculomegaly (Weiss et al., 2020). We found that CHD4 localized to nuclei in mouse ChP epithelial cells beginning at P0 (**Fig. 3B**). Immunoprecipitation of CHD4 identified HDAC1, HDAC2, and MBD3 by immunoblotting in mouse ChP (**Fig. 3C,** technical control for Co-IP protocol is shown in **Supplementary Fig. 7**), confirming the existence of the CHD4/NuRD complex in developing ChP. We then disrupted the

complex by generating ChP-*Chd4* deficient mice. Cre was expressed in *Chd4* floxed mice (*Chd4* fl/fl) (Williams et al., 2004) using an adeno-associated viral vector (AAV) with tropism for the ChP (AAV2/5) (Haddad et al., 2013), delivered by *in utero* intracerebroventricular (ICV) injection at E14.5. *Chd4* transcript levels dropped to <50% by P7 (**Fig. 3D**). While CHD4 protein levels only substantially decreased by P14 (**Fig. 3E, G**), we found that the developmental increase of ChP NKCC1 expression was disrupted as soon as the CHD4 protein decreased and lasted at least until P28 (**Fig. 3F, G**). Similar results were also observed in 4VChP (**Fig. 3H, I**). The expression of other developmentally regulated, functionally relevant candidates (*atp1a1, atp1b1, and klotho*) was not affected (data not shown). These data confirm that the NuRD/ChD4 complex is one of the required components tightly regulating ChP NKCC1 developmental expression.

ChP NKCC1 actively mediates CSF clearance during the early postnatal transition phase

To test whether NKCC1 is indeed capable of transporting from CSF into the ChP during the period of rapid CSF [K^+] decline, we induced NKCC1 overexpression (OE) in developing ChP epithelial cells using AAV2/5. NKCC1 transport directionality follows combined Na^+, K^+, Cl^- gradients, which are close to being neutral in adult brains and likely to bias towards the CSF-to-ChP direction during the early postnatal phase. NKCC1 protein level would be rate-limiting during the early postnatal time when it is already highly phosphorylated, unlike in older mice where pNKCC1 only represented a small portion of total NKCC1. The goal of this OE approach was to accelerate endogenous ChP NKCC1 transport, thereby revealing its directionality based on whether CSF [K^+] clearance was enhanced or delayed. AAV2/5-NKCC1, which expresses NKCC1 fused to an HA tag (Somasekharan et al., 2013), or control GFP virus was delivered by

in utero ICV at E14.5. Successful NKCC1 OE and increased pNKCC1 was confirmed in ChP at P0 (**Fig. 4A-D**). Appropriate localization to apical membranes of epithelial cells, transduction efficiency, and tissue specificity were also validated (**Fig. 4E-I, Supplementary Fig. 8 A, B**). Transcript levels of other K^+ transporters or channels did not change following AAV2/5-NKCC1 transduction (**Supplementary Fig. 8C**). Because CSF [K^+] sharply decreased from P0 to P7 (**Fig. 1A**), we sampled CSF from ChP NKCC1 OE and control mice at P1. We found that ChP NKCC1 OE reduced CSF [K^+] more than controls, with their P1 CSF [K^+] values closely approximating those normally observed at P7 (**Fig. 4J**), indicating accelerated K^+ clearance from CSF after enhanced ChP NKCC1 activity. CSF total protein levels were not affected (AAV2/5-GFP = 2.50 ± 0.20 mg/ml vs. AAV2/5-NKCC1 = 2.71 ± 0.46 mg/ml; N = 6 from two litters each; $p = 0.34$, unpaired t-test). Overall, these findings support a model in which, under physiological conditions with high early postnatal CSF [K^+], ChP NKCC1 transports K^+ out of CSF.

Next, we found that the circulating CSF volume in ChP NKCC1 OE mice was reduced, as reflected by smaller lateral ventricles. To avoid any tissue processing artifacts, we conducted live T2-weighted magnetic resonance imaging (MRI) (**Fig. 5A**) to quantify lateral ventricle volume. AAV-GFP mice were indistinguishable from naive wild-type mice at P14. In contrast, NKCC1 OE mice had reduced lateral ventricle volumes (**Fig. 5A, B**), without decrease in overall brain size (**Fig. 5C**), reflecting less circulating CSF. The difference in ventricle sizes from these same mice was sustained up to our final measurement at P50 (AAV-GFP: 3.12 ± 0.59 mm^3 vs. AAV-NKCC1: 1.28 ± 0.28 mm^3, * $p = 0.0182$). While the exact transport direction of NKCC1 in adult ChP is still under debate (Delpire and Gagnon, 2019), the consistency in ventricular volume from P14 into later life supports our working model that because a relatively small proportion of ChP NKCC1 was phosphorylated in mice P14 and older (**Fig. 2G**), NKCC1 levels

are not rate-limiting and thus OE would not as substantially impact ChP functions in older animals. Collectively, our findings demonstrate that ChP NKCC1 mediated CSF clearance during the first postnatal week. Augmenting this process impacted CSF volume homeostasis in the long term.

We then tested and found that enhancing CSF clearance through ChP NKCC1 OE changed how the brain and cranial space adapted to CSF volume changes. Intracranial compliance (C_i) and CSF resistance (R_{CSF}) describe the ability of the entire intracranial space (including brain, meninges, and outflow routes) to accommodate an increasing CSF volume that would otherwise increase intracranial pressure (ICP). In humans, these parameters are measured by a CSF constant rate infusion test (Aquilina et al., 2012, Eide, 2018, Lalou et al., 2018) and can aid in diagnosis and evaluation of conditions like hydrocephalus, which has decreased C_i (Kahle et al., 2016). We developed a miniaturized version of this test to determine the C_i and R_{CSF} in mice. The constant rate infusion test artificially increases CSF volume by ICV infusion of artificial CSF (aCSF), causing ICP to rise and plateau at a new level (**Fig. 5D, E**). The C_i and R_{CSF} are estimated from the ICP vs. time curve using Marmarou's model of CSF dynamics (Czosnyka et al., 2012) (**Supplementary Fig. 9A**). Simply put, the C_i is proportional to the rate of ICP increase, and the R_{CSF} is related to the level of the post-infusion ICP plateau (**Fig. 5E**). As a quality control for the correct placement of infusion and measurement catheter, arterial and respiratory pulsations were clearly visible in the ICP waveform and their amplitude increased with volume load as expected (**Supplementary Fig. 9B, C**). Using this approach, we found that ChP NKCC1 OE significantly increased C_i at an age of 5-7 weeks (**Fig. 5F, G**), consistent with the brain having greater capacity for CSF in ventricles "deflated" due to excessive CSF clearance. Resting ICP and R_{CSF} were unchanged (**Fig. 5H, I**).

274

275 **Enhanced ChP NKCC1 function mitigates ventriculomegaly in a model of obstructive**
276 **hydrocephalus**

277 Our findings of enhanced CSF clearance after ChP NKCC1 OE indicate that ChP
278 NKCC1 can remove excess CSF. Therefore, we hypothesized that ChP NKCC1 OE expression
279 could mitigate ventriculomegaly in a model of postnatal obstructive hydrocephalus. We first
280 overexpressed ChP NKCC1 at E14.5 by in utero AAV2/5 ICV, then introduced obstructive
281 hydrocephalus by a single unilateral injecting of kaolin into the lateral ventricle at P4 (Shaolin et
282 al., 2015), and finally evaluated the lateral ventricle volumes by live T2 MRI at P14 (**Fig. 6A**).
283 While both NKCC1 OE and control mice had enlarged ventricles at P14, NKCC1 OE mice had
284 reduced ventriculomegaly compared to controls, with the average ventricle volume being less
285 than 1/3 of the controls (**Fig. 6B-D;** ventricles marked by blue arrows; kaolin deposits marked by
286 red arrows). Taken together, our findings demonstrate that early, ChP targeted NKCC1 OE has a
287 sustained and broad impact on specific volumetric and biophysical parameters of the intracranial
288 space with potential therapeutic applications to hydrocephalus.

289

DISCUSSION

In this study we sought to understand how CSF is cleared from the brain before the development of canonical CSF outflow routes (e.g. arachnoid granulations and meningeal lymphatics) (Antila et al., 2017, Munk et al., 2019). The intervening time period is a critical, transient phase in brain development when failure of CSF clearance has debilitating consequences (Volpe, 2008). Our results suggest that this period is defined by rapid decrease in CSF K^+. The ChP mediates the CSF K^+ clearance during this transition period, and thus forms a CSF outflow route through ion and water co-transport by NKCC1 (**Fig. 7**). This CSF clearance by the ChP contrasts the prevailing models that ChP constantly, unidirectionally secretes CSF. Taken together, we discovered an unconventional, precisely timed, function of the developing ChP that clears CSF prior to the formation of other canonical routes, and provides targets for fluid management intervention during a critical transition phase of brain development.

NKCC1 is a bidirectional transporter, recently discovered to be an important co-transporter of water in the adult ChP (Steffensen et al., 2018). Although clearly established as a key molecular mechanism of CSF regulation, ChP NKCC1 transport direction and its determinants *in vivo* have been actively debated due to the technical challenges of 1) specifically manipulating ChP NKCC1 without affecting NKCC1 in other CSF-contacting cells, instead of ICV application of chemicals such as NKCC1 inhibitor bumetanide; and 2) accurately determining intracellular ion levels of ChP epithelial cells, and therefore ion gradients, under physiological conditions, as summarized in **Supplementary Table 1** and reviewed by Delpire and Gagnon (Delpire and Gagnon, 2019). Our *in vivo* "gain-of-function" approach effectively bypasses the abovementioned technical limitations. By overexpressing NKCC1 specifically in the ChP through AAV transduction to amplify its physiological functional impact, we could

subsequently observe the resulting CSF K^+ and fluid volume changes to reveal the transporter's native directionality. Using this approach, we found that, in contrast to the common notion that the ChP constantly produces CSF, NKCC1 in the ChP mediated CSF clearance when CSF [K^+] is above adult values, especially during the first postnatal week in mice. This phase corresponds to the third trimester to 6 months after birth in human, which represents a window of high vulnerability to congenial fluid disorders (Volpe, 2008).

We next demonstrated that the ChP clearance of CSF can be targeted to temper abnormal CSF accumulation. The ChP has been targeted for therapeutic manipulation in rodent models of neurologic diseases ranging from Huntington's disease and lysosomal storage disorders, to Alzheimer's disease, where transduction of exogenous gene products into ependymal or ChP epithelial cells has improved cardinal symptoms of disease (Kaler, 1994, Hudry et al., 2013). Encouragingly, we showed that enhancing ChP epithelial cell NKCC1 transport capacity lessened the severity of ventriculomegaly in a model of obstructive hydrocephalus. Our data demonstrate the possibility of tempering congenital hydrocephalus by augmenting endogenous ChP NKCC1 activity to increase CSF absorption rates during early development when CSF [K^+] is high. In addition, because ChP CSF absorption via NKCC1 is driven by increased CSF [K^+], this mechanism may come into play in other pathogenic conditions where CSF [K^+] is transiently increased, such as after tissue injury or ventricular bleeding. Therefore, our findings emphasize the ChP as a targetable, K^+-sensitive and on-demand CSF drainage route in neurological disorders where CSF homeostasis is disrupted.

Further, in light of recent findings reporting hydrocephalus and ventriculomegaly in children with *de novo* loss-of-function CHD4 mutations (Weiss et al., 2020), we found that the CHD4/NuRD complex is required for the developmental regulation of NKCC1 expression. This

connection suggests a possible pathophysiological mechanism whereby lack of CHD4 activity might reduce NKCC1 levels during early development (equivalent to P0-P7 in mice), and lead to insufficient CSF clearance resulting in hydrocephalus. In our loxP-cre approach, most CHD4 protein knockdown and resulting stagnation of NKCC1 expression occurred by P14, which is beyond the critical window of NKCC1 activity at P0-P7. As such, we did not model developmental ventriculomegaly with this approach. Improved genetic tools for early CHD4 knockout and new animal models harboring the *de novo* patient mutations would be required to fully unravel the regulatory connection between CHD4/NuRD complex and NKCC1.

A key question that emerges from this work is: If the ChP is acting as an outflow pathway rather than a source of CSF during this transitional developmental phase – where does the early CSF water content come from? One mechanism that could be acting at this stage is CSF secretion by the developing brain tissue (e.g. progenitor cells that have a cell body at the ventricular zone but extend their basal processes to the developing pia) which secretes CSF immediately after neural tube closure (Gato et al., 2014). Future studies should elucidate whether this mechanism extends into this transitional phase. Consistent with progenitor involvement in CSF dynamics, recent identification of genes driving pediatric hydrocephalus shows affected genes to be expressed predominantly by cortical progenitor cells lining the brain's ventricles (Furey et al., 2018), and not the ChP, suggesting a non-choroidal source of CSF as an alternative contributor to abnormal CSF production.

In addition to fluid regulation, the newly identified ChP clearance route provides a key mechanism to regulate extracellular K^+ during the first postnatal week. The subunits of the major system for moving K^+ against its individual concentration gradient, the Na^+/K^+-ATPase (i.e. Atp1a1 and Atp1b1), were not yet at their full expression levels during this period. The ChP

NKCC1-mediated K^+ clearance mechanism might assist in establishing the K^+ gradient in a timely manner, which is crucial for cellular physiology (Rasmussen et al., 2020). Notably, the period of rapidly decreasing CSF [K^+] overlaps with the developmental phase when the excitatory-to-inhibitory "GABA switch" occurs. In early cortical progenitor cells that reside in the ventricular zone and are bathed by CSF, the classic inhibitory neurotransmitter GABA leads to excitatory potentials and suppression of DNA synthesis (LoTurco et al., 1995). As newborn cortical neurons differentiate and migrate away from the ventricular zone, GABA switches to adopt the more classic role as an inhibitory neurotransmitter by lowering intracellular Cl^- (Owens et al., 1999) which is achieved through coordinated activities of neuronal K^+/Cl^- co-transporters KCC2 and NKCC1 (Pisella et al., 2019, Watanabe et al., 2019). Because ions, including K^+, can traffic from CSF into interstitial fluid (Cserr, 1965, Fencl et al., 1966), any interference with the developmental timeline of ChP NKCC1 that resulted in delayed CSF K^+ clearance could potentially increase extracellular/interstitial fluid [K^+] and affect neural physiology (Rasmussen et al., 2020). Specifically, such a change in extracellular/interstitial fluid [K^+] could fundamentally impact neuronal NKCC1 and KCC2 transport equilibrium, potentially contributing to a delayed GABA switch, a phenomenon reported in many models of neurodevelopmental and psychiatric disorders including subtypes of autism spectrum disorder (Amin et al., 2017), Rett syndrome (Banerjee et al., 2016), Fragile X syndrome (He et al., 2014), schizophrenia (Hyde et al., 2011), and Down syndrome (Deidda et al., 2015). Furthermore, extracellular [K^+] and certain K^+ channels also regulate activities of microglia (Madry et al., 2018), which are critical in synaptic pruning during postnatal neurodevelopment in mice (Schafer et al., 2012). Thus, the ChP is poised to play important roles in proper CNS formation by creating and maintaining desirable extracellular ionic homeostasis at different developmental

382 stages, with subsequent effects on neuronal maturation, circuit formation, and
383 neuroinflammatory homeostasis.

384 Beyond key findings and implications during this critical transitional developmental stage,
385 our study introduced a murine ICP measurement device combined with constant CSF infusion.
386 This approach provides a much-needed advance in fluid research technology that can be broadly
387 applied to study essentially all CSF dynamic systems across the mouse lifespan. We adapted our
388 tool from clinical practice to provide a range of options for measuring global cerebral fluid states
389 that reflect the interaction between CSF and cranial tissues. In later life, CSF homeostasis is
390 maintained by collaborative efforts from multiple players in the brain, including the ChP, the
391 dural lymphatics (Antila et al., 2017), glymphatics (Munk et al., 2019), leptomeningeal
392 vasculature (Li et al., 2020), and the ependyma (Spassky et al., 2005). While this approach
393 measures overall cranial fluid dynamics as one single unit, future applications could apply
394 mathematical models that have been proposed to isolate the contribution of distinct CSF outflow
395 routes using data acquired from human patients (Vinje et al., 2020). Such adaptability secures the
396 broadening relevance of our tool and inspires optimism for further improved resolution in
397 studying brain fluid dynamics. Availability of this new tool also allows future researchers to
398 obtain measurements in support of the growing comprehensive "systems" view of regulatory
399 mechanisms of CSF-brain interactions.

400 In summary, our study presents a critical transient phase when the ChP acts as a non-
401 canonical route for CSF clearance prior to the maturation of other canonical clearance pathways.
402 ChP NKCC1 mediates CSF clearance in a K^+-dependent manner. Targeting this absorption route
403 holds promise in improving fluid management for congenital hydrocephalus and other CSF
404 disorders.

405 **ACKNOWLEDGEMENTS**

406 We thank members of the Lehtinen, Heiman, and Warf labs for helpful discussions;
407 Nancy Chamberlin for critical reading of the manuscript; Katia Georgopoulos for sharing the
408 *Chd4* fl/fl mouse line and associated genotyping methods; P. Ellen Grant for the ICP monitor.
409 We thank the following facility and personnel: Maria Ericsson and HMS EM facility; Yaotang
410 Wu and Michael Marcotrigiano and BCH Small Animal Imaging Laboratory; the MIT BioMicro
411 Center (TRAP sequencing); BCH viral core and University of Pennsylvania Vector Core.

412 Funding: NIH T32 HL110852 (RMF and JC); William Randolph Hearst Fund (JC); NSF
413 Graduate Research Fellowship Program (FBS); OFD/BTREC/CTREC Faculty Development
414 Fellowship Award (RMF); Simons Foundation Autism Research Awards (IDs 590293 and
415 645596 for CN and DS, respectively). NIH R01 AI130591 and R35 HL145242 (MJH); NIH R00
416 HD083512 (P-YL) and R01 HD096693 (P-YL & BCW); BCH Pilot Grant, Pediatric
417 Hydrocephalus Foundation, Hydrocephalus Association, Human Frontier Science Program
418 (HFSP) research program grant #RGP0063/2018, NIH R01 NS088566, the New York Stem Cell
419 Foundation (MKL); and BCH IDDRC 1U54HD090255. M.K. Lehtinen is a New York Stem Cell
420 Foundation – Robertson Investigator.

421

422 **Author contributions:** H.X., R.M.F., C.S. J.S., P.-Y. L., B.C.W., F.B.S., J.C., D.S., C.N., and
423 M.K.L. designed and performed experiments; H.X., R.M.F., C.S., and J.S. analyzed the data;
424 Y.Z. and M.J.H. provided material; A.V., F.G., and M.H. provided technological support; H.X.,
425 R.M.F., and M.K.L. wrote the manuscript. All co-authors edited the manuscript.

426

427 **Declaration of interests:** The authors declare that no competing interests exist.

METHODS

Mice

The Boston Children's Hospital IACUC approved all experiments involving mice in this study. Timed pregnant CD1 dams were obtained from Charles River Laboratories. Mice with germline loxP-CHD4-loxP were imported from MGH and bred in-house. Both male and female mice were equally included in the study and were analyzed at postnatal day 0, 7, 14, 21, 28, 5-7weeks, and 2+ months. Animals were housed in a temperature-controlled room on a 12-hr light/12-hr dark cycle and had free access to food and water. For studies involving mice younger than postnatal day 10, all mice were allocated into groups based solely on the gestational age without respect to sex (both males and females were included). For studies involving mice older than 10 days, both male and female are included intentionally.

CSF Collection and Metal Detection

CSF was collected by from cisterna magna using a glass capillary, and collected CSF was centrifuged at 10,000xg for 10min at 4℃ to remove any tissue debris. Metal quantifications were performed by Galbraith Laboratories, Inc. (Knoxville, TN, USA). Inductively coupled plasma - optical emission spectrometry (ICP-OES) was used for K and Na quantification, and ion chromatography (IC) was used for the Cl^- quantification. All tests were performed using 5-7μL of CSF.

TRAP

Mice aged 8 weeks or E16.5 from the *Foxj1*:Cre x EGFP-L10a Bacterial Artificial Chromosome (BAC) transgenic lines (N=3, each N included LVChP pooled from 3 mice) were used and brain tissue was immediately dissected and used for TRAP RNA purifications as

previously described (Heiman et al., 2008). RNA quality was assessed using Bioanalyzer Pico Chips (Agilent, 5067-1513) and quantified using Quant-iT RiboGreen RNA assay kit (Thermo Fisher Scientific R11490). Libraries were prepared using Clonetech SMARTer Pico with ribodepletion and Illumina HiSeq to 50NT single end reads. Sequencing was performed at the MIT BioMicroCenter.

Sequencing Data Analysis

The raw fastq data of 50-bp single-end sequencing reads were aligned to the mouse mm10 reference genome using STAR 2.4.0 RNA-Seq aligner (Dobin et al., 2013). The mapped reads were processed by htseq-count of HTSeq software (Anders et al., 2015) with mm10 gene annotation to count the number of reads mapped to each gene. The Cuffquant module of the Cufflinks software (Trapnell et al., 2010) was used to calculate gene FPKM (Fragments Per Kilobase of transcript per Million mapped reads) values. Gene differential expression test between different animal groups was performed using DESeq2 package (Love et al., 2014) with the assumption of negative binomial distribution for RNA-Seq data. Genes with adjusted p-value< 0.05 are chosen as differentially expressed genes. All analyses were performed using genes with FPKM> 1, which we considered as the threshold of expression (Figure 2- source data).

Sequencing Pathway and Motif Analysis

Functional annotation clustering was performed using DAVID v6.7 (Huang da et al., 2009). Gene ontology (GO) analysis was performed using AdvaitaBio iPathway guide V.v1702. Enrichment vs. perturbation analysis was performed by AdvaitaBio iPathway guide V.v1702 and allows comparison of pathway output perturbation and cumulative gene set expression changes. In brief, the enrichment analysis is a straightforward gene-set enrichment over representation

473 analysis (ORA) considering the number of differentially expressed genes (DEGs) that are
474 assigned to a given pathway. The enrichment value is expressed as a proportion of enriched
475 members to total genes in a defined pathway and a p-value (Fisher) is calculated for this score,
476 however false positives have been reported at up to 10% with this method (Draghici et al., 2007).
477 Perturbation, on the other hand, uses pathway data that applies relationships between gene
478 products rather than only using a list. Perturbation assigns an impact score based on a
479 mathematical model that captures the entire topology of the pathway and uses it to calculate how
480 changes in the expression of each gene in the pathway would perturb the absolute output of the
481 pathway (Draghici et al., 2007). Then, these gene perturbations are combined into a total
482 perturbation for the entire pathway and a p-value is calculated by comparing the observed value
483 with what is expected by chance. Motif analyses were performed using SignalP (v5.0; Almagro
484 Armenteros et al., 2019) and TMHMM (v2.0; Sonnhammer et al., 1998).

485 Transmission Electron Microscopy

486 All tissue processing, sectioning, and imaging was carried out at the Conventional
487 Electron Microscopy Facility at Harvard Medical School. Forebrain tissues were fixed in 2.5%
488 Glutaraldehyde/2% Paraformaldehyde in 0.1 M sodium cacodylate buffer (pH 7.4). They were
489 then washed in 0.1M cacodylate buffer and postfixed with 1% Osmiumtetroxide (OsO4)/1.5%
490 Potassiumferrocyanide ($KFeCN_6$) for one hour, washed in water three times and incubated in 1%
491 aqueous uranyl acetate for one hour. This was followed by two washes in water and subsequent
492 dehydration in grades of alcohol (10 minutes each; 50%, 70%, 90%, 2x10min 100%). Samples
493 were then incubated in propyleneoxide for one hour and infiltrated overnight in a 1:1 mixture of
494 propyleneoxide and TAAB Epon (Marivac Canada Inc. St. Laurent, Canada). The following day,
495 the samples were embedded in TAAB Epon and polymerized at 60 degrees C for 48 hours.

Ultrathin sections (about 80nm) were cut on a Reichert Ultracut-S microtome, and picked up onto copper grids stained with lead citrate. Sections were examined in a JEOL 1200EX Transmission electron microscope or a TecnaiG² Spirit BioTWIN. Images were recorded with an AMT 2k CCD camera.

Glycogen and Mitochondrial Quantification

Glycogen and mitochondrial quantification was performed by hand using the ImageJ plugin FIJI (Schindelin et al., 2012, Schneider et al., 2012). Percentages were calculated by dividing the area of interest by the total area of ChP epithelial cell within the field of view. No other cell types were included in the analysis. For each condition, analyses were performed across multiple individual animals (N=3 for each age). From each animal, 10-20 fields of view were imaged at 3,000x for glycogen analysis and 5-10 fields of view were imaged at 3,000x for mitochondrial analysis. Each different field of view represented a unique cell or cells, and fields of view were chosen such that both the apical and basal surfaces of the cell were visible. For mitochondrial distribution, a custom MatLab (v.2018) code was written to extract the centroid from mitochondria data traced in ImageJ ROIs (Supplementary file). Then a distance transformation was performed from each mitochondrion centroid to the hand-traced apical or basal surfaces. The shortest distance was extracted to calculate the apical: basal proximity ratio, such that 1= on the apical surface and 0= on the basal surface. The analyses included a total of 1747 adult mitochondria, 2241 P7 mitochondria, 2257 P0 mitochondria, and 1123 embryonic mitochondria.

Seahorse Metabolic Analysis

ChP explants were dissected in HBSS (Fisher, SH30031FS) and maintained on wet ice

until plated. Only the posterior leaflet of the P0, P7, and adult ChP was retained for analysis due to empirically determined limitations of the oxygen availability in the XFe96 Agilent Seahorse system. Tissue explants were plated on Seahorse XFe96 spheroid microplates (Agilent, 102905-100) coated with Cell TAK (Corning), in Seahorse XF Base Medium (Agilent, 102353-100) supplemented with 0.18% glucose, 1mM L-glutamine, and 1mM pyruvate at pH7.4 and incubated for 1 hour at 37 °C in a non-CO_2 incubator. Extracellular acidification rates (ECAR) and oxygen consumption rates (OCR) were measured via the Cell Mito Stress Test (Agilent, 103015-100) with a Seahorse XFe96Analyzer (Agilent) following the manufacturer's protocols. Data were processed using Wave software (Agilent). ATP production was calculated as the difference in OCR measurements before and after oligomycin injection, as described by the manufacturer's protocol (Agilent, 103015-100). The Cell Mito Stress test was performed 2-5 independent times. The individual analyses were performed by averaging the readings from both the right and left hemisphere lateral ventricle ChP for each individual. Data were normalized by Calcein-AM (2μM in PBS, Life Technologies L-3224) fluorescence measured at the end of the assay. Data are presented normalized to the adult levels for each assay to account for any experimental variability.

High K^+ challenge study

Fresh LV ChPs were collected from P4 pups and adult mice in room temperature HBSS and glued down onto imaging dishes with coverslip bottom. The tissues were incubated at 37 °C with Calcein-AM (Invitrogen L3224; 1:200) for 10min and then rinsed with 37 °C artificial CSF (aCSF: 119 mM NaCl, 2.5 mM KCl, 26 mM $NaHCO_3$, 1 mM NaH_2PO_4, 11 mM glucose, with fresh 2.0 mM magnesium chloride and 2.8 mM calcium chloride). The tissues were soaked in 1.8ml aCSF at the beginning of each imaging session and allowed to stabilize for 10min. One Z-

stack was acquired to reflect the baseline cell volume. Then a 10x KCl solution in aCSF was spiked into the bath to make the final bath K^+ concentration 50mM immediately before imaging subsequent continued. A total of five 3D Z-stacks were acquired throughout a 10-min imaging session to capture changes in cellular volume over time. Each stack took less than 30s to minimize changes in cell volume from the beginning to the end of each stack. All imaging studies were carried out at 37°C. Image stacks were imported into Imaris (Bitplane) software. Individual epithelial cells were identified by shape. Cells with discrete borders that were present at all timepoints and had dark pixels both above and below them in Z for the whole timecourse were selected *a priori* and then traced by hand using the "Surpass" functionality to create a 3D surface volume through all Z stacks based on Calcein-AM uptake signal. Due to known z-step distance and interpolation between the planes, Imaris calculated the number of voxels for each cell. This analysis was then repeated for the same cell throughout the timecourse. We verified manually that the cell was the same individual based on the topology of the surrounding cells, allowing for adjustment for any x-y drifting that occurred. The relative volume was calculated as dV/V_0 for each timepoint (t) where V_0 is the initial volume of the cell, t is each subsequent timepoint after addition of challenge, and $dV = Vt-V_0$.

Tissue processing

Samples were fixed in 4% paraformaldehyde (PFA). For cryosectioning, samples were incubated in the following series of solutions: 10% sucrose, 20% sucrose, 30% sucrose, 1:1 mixture of 30% sucrose and OCT (overnight), and OCT (1 hour). Samples were frozen in OCT.

Immunostaining

Cryosections were blocked and permeabilized (0.3% Triton-X-100 in PBS; 5% serum), incubated in primary antibodies overnight and secondary antibodies for 2 hours. Sections were

564 counterstained with Hoechst 33342 (Invitrogen H3570, 1:10000) and mounted using
565 Fluoromount-G (SouthernBiotech). The following primary antibodies were used: chicken anti-
566 GFP (Abcam ab13970; 1:1000), mouse anti-Aqp1 (Santa Cruz sc-32737; 1:100), rabbit anti-
567 CHD4 (Abcam ab72418, 1:200), rabbit anti-NKCC1 (Abcam ab59791; 1:500), rat anti-HA
568 (Roche 11867423001; 1:1000). Secondary antibodies were selected from the Alexa series
569 (Invitrogen, 1:500). Images were acquired using Zeiss LSM880 confocal microscope with 20x
570 objective.

571 Co-IP

572 Tissues were homogenized in NET buffer (150mM NaCl, 10mM Tris 8.0, 5mM EDTA,
573 10% glycerol and 2% Triton-100) supplemented with protease inhibitors. Protein concentration
574 was determined by BCA assay (Thermo Scientific 23227). Lysates with same amount of total
575 protein (250-1000µg based on experiments) were pre-cleared at 4° C for 2hr with Protein G
576 agarose and then incubated with desired antibody or control antibody at 4° C overnight (no beads
577 present during antibody incubation). Protein G agarose beads were added to lysate-antibody
578 mixture after overnight incubation for 2hr. Beads were washed thoroughly and then eluted by
579 boiling in 2% SDS. ChP tissues were pooled across 7 litters of P0 pups and 30 adults to achieve
580 sufficient protein for Co-IP.

581 Immunoblotting

582 Tissues were homogenized in RIPA buffer supplemented with protease and phosphatase
583 inhibitors. Protein concentration was determined by BCA assay (Thermo Scientific 23227).
584 Samples were denatured in 2% SDS with 2-mercaptoethanol by heating at 37°C (for NKCC1) or
585 95°C (for CHD4 and other NuRD complex proteins) for 5 minutes. Equal amounts of proteins
586 were loaded and separated by electrophoresis in a 4-15% gradient polyacrylamide gel (BioRad

#1653320) or NuPAGE 4-12% Bis-Tris gel (Invitrogen #NP0322), transferred to a nitrocellulose membrane (250mA, 1.5 hours, on ice), blocked in filtered 5% BSA or milk in TBST, incubated with primary antibodies overnight at 4°C followed by HRP conjugated secondary antibodies (1:5000) for 1 hour, and visualized with ECL substrate. For phosphorylated protein analysis, the phospho-proteins were probed first, and then blots were stripped (Thermo Scientific 21059) and reprobed for total proteins. For co-IP protein analysis, TrueBlot secondary antibody (eBioscience 18-8816-33) was used to detect only non-denatured IgG and avoid background signal from IP antibody. The following primary antibodies were used: rabbit anti-NKCC1 (Abcam ab59791; 1:1000), rabbit anti-pNKCC1 (EMD Millipore ABS1004; 1:1000), rabbit anti-ATP1a1 (Upstate C464.6/05-369; 1:250, goat-anti-klotho (R&D AF1819-sp; 1:200), rabbit anti-GAPDH (Sigma G9545; 1:10000), mouse anti-HA (Abcam ab130275; 1:1000), rabbit anti-CHD4 (Abcam ab72418; 1:2000), rabbit anti-MBD3 (Abcam ab157464; 1:1000), rabbit anti-HDAC1 (Abcam ab7028; 1:2000), mouse anti-HDAC2 (Abcam 51832; 1:2000).

Quantitative RT-PCR

For mRNA expression analyses, the ChP were collected and pooled from 2 pups. RNA was isolated using the MirVana miRNA isolation kit (Invitrogen AM1561) following manufacturer's specifications without miRNA enrichment step. Extracted RNA was quantified spectrophotometrically and 100ng was reverse-transcribed into cDNA using the High Capacity cDNA Reverse Transcription kit (Applied Biosystems #4368814) following manufacturer's specifications. RT-qPCRs were performed in duplicate using Taqman Gene Expression Assays and Taqman Gene Expression Master Mix (Applied Biosystems) with GAPDH as an internal control. Cycling was executed using the StepOnePlus Real-Time PCR System (Invitrogen) and analysis of relative gene expression was performed using the $2^{-\Delta\Delta CT}$ method. Technical replicates

were averaged for their cycling thresholds and further calculations were performed with those means.

In utero intracerebroventricular injection (ICV)

Timed pregnant mice (E14.5) were deeply anesthetized by isoflurane and placed on warm pads. Laparotomy was performed and AAV solution was delivered into the lateral ventricle of each embryo using glass capillary pipettes. The abdominal incision was then sutured. Meloxicam analgesia was longitudinally delivered according to IACUC protocol.

Intraventricular kaolin injection in postnatal pups

Postnatal day 4 pups (P4) were deeply anesthetized by hypothermia. 1µl of sterile kaolin solution (25% in PBS) was delivered into the left lateral ventricle using glass capillary pipettes. The lateral ventricle location was determined as in between bregma and lambda, and 1mm from mid-line. The pups were then warmed and returned to the dam.

AAV production

The original AAV-NKCC1 plasmid was purchased from Addgene (pcDNA3.1 HA CFP hNKCC1 WT (NT15-H) was a gift from Biff Forbush: Addgene plasmid # 49077; http://n2t.net/addgene:49077; RRID:Addgene_49077). The plasmid carries an 3xHA tag at the N-terminal of NKCC1 to allow detection and separation from endogenous NKCC1. The CFP tag was removed by BsaI digestion to reduce insert size for AAV production. Virus production and purification were performed by the Penn Vector Core. Due to the very large size of the plasmid we experienced variable infection efficiency. All mice receiving AAV-NKCC1 were analyzed for HA expression after every experiment to confirm infection efficiency. AAV-GFP and AAV-Cre were purchased from BCH viral core at Boston Children's Hospital.

Magnetic resonance imaging (MRI)

Mice were imaged using Bruker BioSpec small animal MRI (7T) at 2wk and P50 while under anesthesia by isoflurane. A warm pad was used to maintain body temperature. Breathing rate and heart rate were monitored to reflect the depth of anesthesia. All axial T2 images were acquired using the following criteria: TE/TR=60/4000; Ave=8; RARE=4; slice thickness=0.6mm. Ventricle volumes were calculated by manual segmentation using FIJI/ImageJ. In studies with unilateral kaolin injection, 3D reconstruction of the ventricles was performed by manual segmentation in ITK-SNAP (Madan, 2015) and exported through ParaView.

Constant rate CSF infusion test (ICP and compliance measurement)

An apparatus was developed to perform a constant infusion test in mice through a single catheter for both infusion of CSF and monitoring of ICP. A 20cc syringe was filled with aCSF and placed in an automated infusion pump (GenieTouch, Kent Scientific Co., Denver) and set to deliver a constant rate infusion of 1-4 uL/minute. The syringe was connected via pressure tubing to hemostasis valve Y connector (Qosina, NY). A fiberoptic ICP sensor (Fiso Technologies Inc, Québec, Canada) was inserted through the other port of the rotating hemostat and then into 0.55 mm diameter catheter until the sensor was flush with the catheter's distal tip. The entire apparatus and tubing was carefully screened to ensure the absence of air bubbles. Adult mice were then deeply anesthetized, placed on a warm pad, and head-fixed with ear bars. The distal end of the infusion device (catheter with fiberoptic sensor) was placed inside lateral ventricle (-0.4mm (anterior-posterior) and 1.2mm (medial-lateral) with respect to Bregma, and a depth of 2 mm from the outer edge of the skull); the catheter was then sealed with Vetbond (3M, Minnesota). Intraventricular access and water-tight seal was confirmed by observation of arterial and respiratory waveforms in the ICP signal and a transient rise in ICP upon gentle compression

of the abdomen and thorax. Two minutes of baseline ICP were recorded before initiating the infusion of aCSF. As the infusion proceeded, careful observation was made of the mouse's respiratory rate. After the ICP level reached a new plateau, the infusion was discontinued. The procedure was terminal. Parameters of the Marmarou model of CSF dynamics for constant rate infusions were estimated by a non-linear least squares fit of the model to the ICP data (Czosnyka et al., 2012)

$$ICP(t) = \frac{\left[i_{infusion} + \frac{ICP_{baseline} - p_0}{R_{CSF}}\right] \cdot [ICP_{baseline} - p_0]}{\frac{ICP_{baseline} - p_0}{R_{CSF}} + i_{infusion} \cdot \left[e^{-\frac{\left[i_{infusion} + \frac{ICP_{baseline} - p_0}{R_{CSF}}\right].}{C_i} t}\right]}$$

where $i_{infusion}$ is the rate of infusion, $ICP_{baseline}$ is the ICP level before infusion, p_0 is a pressure in the storage arm of the model, R_{CSF} is the resistance to CSF outflow, and C_i is the compliance coefficient.

QUANTIFICATION AND STATISTICAL ANALYSIS

Biological replicates (N) were defined as samples from distinct individual animals, analyzed either in the same experiment or within multiple experiments, with the exception when individual animal could not provide sufficient sample (i.e. CSF), in which case multiple animals were pooled into one biological replicate and the details are stated in the corresponding figure legends. Statistical analyses were performed using Prism 7 or R. Outliers were excluded using ROUT method (Q = 1%). Appropriate statistical tests were selected based on the distribution of data, homogeneity of variances, and sample size. The majority of the analyses were done using One-way ANOVA with multiple comparison correction (Sidak) or Welch's unpaired t-test, except for Fig. 1E-G, and Fig. 1I-J where the analysis was done by Welch's ANOVA with Dunnett's T3 multiple comparison test, and Fig. 1L where the analysis was done using

675 Kolmogorov-Smirnov test. F tests or Bartlett's tests were used to assess homogeneity of
676 variances between data sets. Parametric tests (t-test, ANOVA) were used only if data were
677 normally distributed and variances were approximately equal. Otherwise, nonparametric
678 alternatives were chosen. Data are presented as means ± standard deviation (SD). If multiple
679 measurements were taken from a single individual, data are presented as means ± standard errors
680 of the mean (SEMs). Please refer to figure legends for sample size. p values < 0.05 were
681 considered significant (* $p < 0.05$, ** $p < 0.01$, *** $p < 0.001$, **** $p < 0.0001$). Exact p values
682 can be found in the figure legends. P values are also marked in the figures where space allows.
683

REFERENCES:

Almagro Armenteros JJ, Tsirigos KD, Sonderby CK, Petersen TN, Winther O, Brunak S, von Heijne G, Nielsen H (2019) SignalP 5.0 improves signal peptide predictions using deep neural networks. *Nature biotechnology* 37:420-423.

Amin H, Marinaro F, De Pietri Tonelli D, Berdondini L (2017) Developmental excitatory-to-inhibitory GABA-polarity switch is disrupted in 22q11.2 deletion syndrome: a potential target for clinical therapeutics. *Scientific reports* 7:15752.

Anders S, Pyl PT, Huber W (2015) HTSeq--a Python framework to work with high-throughput sequencing data. *Bioinformatics* 31:166-169.

Antila S, Karaman S, Nurmi H, Airavaara M, Voutilainen MH, Mathivet T, Chilov D, Li Z, Koppinen T, Park JH, Fang S, Aspelund A, Saarma M, Eichmann A, Thomas JL, Alitalo K (2017) Development and plasticity of meningeal lymphatic vessels. *The Journal of experimental medicine* 214:3645-3667.

Aquilina K, Pople IK, Sacree J, Carter MR, Edwards RJ (2012) The constant flow ventricular infusion test: a simple and useful study in the diagnosis of third ventriculostomy failure. *Journal of neurosurgery* 116:445-452.

Banerjee A, Rikhye RV, Breton-Provencher V, Tang X, Li C, Li K, Runyan CA, Fu Z, Jaenisch R, Sur M (2016) Jointly reduced inhibition and excitation underlies circuit-wide changes in cortical processing in Rett syndrome. *Proceedings of the National Academy of Sciences of the United States of America* 113:E7287-E7296.

Bhargava P, Schnellmann RG (2017) Mitochondrial energetics in the kidney. *Nature reviews Nephrology* 13:629-646.

Cserr H (1965) Potassium exchange between cerebrospinal fluid, plasma, and brain. *The American journal of physiology* 209:1219-1226.

Czosnyka M, Czosnyka Z, Agarwal-Harding KJ, Pickard JD (2012) Modeling of CSF dynamics: legacy of Professor Anthony Marmarou. *Acta neurochirurgica Supplement* 113:9-14.

Damkier HH, Brown PD, Praetorius J (2013) Cerebrospinal fluid secretion by the choroid plexus. *Physiological reviews* 93:1847-1892.

Darman RB, Forbush B (2002) A regulatory locus of phosphorylation in the N terminus of the Na-K-Cl cotransporter, NKCC1. *The Journal of biological chemistry* 277:37542-37550.

Deidda G, Parrini M, Naskar S, Bozarth IF, Contestabile A, Cancedda L (2015) Reversing excitatory GABAAR signaling restores synaptic plasticity and memory in a mouse model of Down syndrome. *Nature medicine* 21:318-326.

Delpire E, Gagnon KB (2019) Elusive role of the Na-K-2Cl cotransporter in the choroid plexus. *American journal of physiology Cell physiology* 316:C522-C524.

Dobin A, Davis CA, Schlesinger F, Drenkow J, Zaleski C, Jha S, Batut P, Chaisson M, Gingeras TR (2013) STAR: ultrafast universal RNA-seq aligner. *Bioinformatics* 29:15-21.

Draghici S, Khatri P, Tarca AL, Amin K, Done A, Voichita C, Georgescu C, Romero R (2007) A systems biology approach for pathway level analysis. *Genome research* 17:1537-1545.

Eide PK (2018) The pathophysiology of chronic noncommunicating hydrocephalus: lessons from continuous intracranial pressure monitoring and ventricular infusion testing. *Journal of neurosurgery* 129:220-233.

Fame RM, Lehtinen MK (2020) Emergence and Developmental Roles of the Cerebrospinal Fluid System. *Developmental Cell* 52:261-275.

Fencl V, Miller TB, Pappenheimer JR (1966) Studies on the respiratory response to disturbances of acid-base balance, with deductions concerning the ionic composition of cerebral interstitial fluid. *The American journal of physiology* 210:459-472.

Furey CG, Choi J, Jin SC, Zeng X, Timberlake AT, Nelson-Williams C, Mansuri MS, Lu Q, Duran D, Panchagnula S, Allocco A, Karimy JK, Khanna A, Gaillard JR, DeSpenza T, Antwi P, Loring E, Butler WE, Smith ER, Warf BC, Strahle JM, Limbrick DD, Storm PB, Heuer G, Jackson EM, Iskandar BJ, Johnston JM, Tikhonova I, Castaldi C, Lopez-Giraldez F, Bjornson RD, Knight JR, Bilguvar K, Mane S, Alper SL, Haider S, Guclu B, Bayri Y, Sahin Y, Apuzzo MLJ, Duncan CC, DiLuna ML, Gunel M, Lifton RP, Kahle KT (2018) De Novo Mutation in Genes Regulating Neural Stem Cell Fate in Human Congenital Hydrocephalus. *Neuron* 99:302-314 e304.

Gato A, Alonso MI, Martin C, Carnicero E, Moro JA, De la Mano A, Fernandez JM, Lamus F, Desmond ME (2014) Embryonic cerebrospinal fluid in brain development: neural progenitor control. *Croatian medical journal* 55:299-305.

Gilmore JH, Kang C, Evans DD, Wolfe HM, Smith JK, Lieberman JA, Lin W, Hamer RM, Styner M, Gerig G (2010) Prenatal and neonatal brain structure and white matter maturation in children at high risk for schizophrenia. *The American journal of psychiatry* 167:1083-1091.

Goodman JV, Bonni A (2019) Regulation of neuronal connectivity in the mammalian brain by chromatin remodeling. *Current opinion in neurobiology* 59:59-68.

Haddad MR, Donsante A, Zerfas P, Kaler SG (2013) Fetal Brain-directed AAV Gene Therapy Results in Rapid, Robust, and Persistent Transduction of Mouse Choroid Plexus Epithelia. *Molecular therapy Nucleic acids* 2:e101.

Hamann S, Herrera-Perez JJ, Zeuthen T, Alvarez-Leefmans FJ (2010) Cotransport of water by the Na+-K+-2Cl(-) cotransporter NKCC1 in mammalian epithelial cells. *The Journal of physiology* 588:4089-4101.

He Q, Nomura T, Xu J, Contractor A (2014) The developmental switch in GABA polarity is delayed in fragile X mice. *The Journal of neuroscience : the official journal of the Society for Neuroscience* 34:446-450.

Heiman M, Schaefer A, Gong S, Peterson JD, Day M, Ramsey KE, Suarez-Farinas M, Schwarz C, Stephan DA, Surmeier DJ, Greengard P, Heintz N (2008) A translational profiling approach for the molecular characterization of CNS cell types. *Cell* 135:738-748.

Huang da W, Sherman BT, Lempicki RA (2009) Systematic and integrative analysis of large gene lists using DAVID bioinformatics resources. *Nature protocols* 4:44-57.

Hudry E, Dashkoff J, Roe AD, Takeda S, Koffie RM, Hashimoto T, Scheel M, Spires-Jones T, Arbel-Ornath M, Betensky R, Davidson BL, Hyman BT (2013) Gene transfer of human

764 Apoe isoforms results in differential modulation of amyloid deposition and neurotoxicity
765 in mouse brain. *Science translational medicine* 5:212ra161.

766 Hyde TM, Lipska BK, Ali T, Mathew SV, Law AJ, Metitiri OE, Straub RE, Ye T, Colantuoni C,
767 Herman MM, Bigelow LB, Weinberger DR, Kleinman JE (2011) Expression of GABA
768 signaling molecules KCC2, NKCC1, and GAD1 in cortical development and
769 schizophrenia. *The Journal of neuroscience : the official journal of the Society for*
770 *Neuroscience* 31:11088-11095.

771 Kahle KT, Kulkarni AV, Limbrick DD, Jr., Warf BC (2016) Hydrocephalus in children. *Lancet*
772 387:788-799.

773 Kaler SG (1994) Menkes disease. *Advances in pediatrics* 41:263-304.

774 Keep RF, Jones HC (1990) A morphometric study on the development of the lateral ventricle
775 choroid plexus, choroid plexus capillaries and ventricular ependyma in the rat. *Brain*
776 *research Developmental brain research* 56:47-53.

777 Lalou AD, Czosnyka M, Donnelly J, Pickard JD, FmedSci, Nabbanja E, Keong NC, Garnett M,
778 Czosnyka ZH (2018) Cerebral autoregulation, cerebrospinal fluid outflow resistance, and
779 outcome following cerebrospinal fluid diversion in normal pressure hydrocephalus.
780 *Journal of neurosurgery* 130:154-162.

781 Li Q, Aalling NN, Forstera B, Erturk A, Nedergaard M, Mollgard K, Xavier ALR (2020)
782 Aquaporin 1 and the Na(+)/K(+)/2Cl(-) cotransporter 1 are present in the leptomeningeal
783 vasculature of the adult rodent central nervous system. *Fluids and barriers of the CNS*
784 17:15.

785 Liddelow SA, Dziegielewska KM, Ek CJ, Habgood MD, Bauer H, Bauer HC, Lindsay H,
786 Wakefield MJ, Strazielle N, Kratzer I, Mollgard K, Ghersi-Egea JF, Saunders NR (2013)
787 Mechanisms that determine the internal environment of the developing brain: a
788 transcriptomic, functional and ultrastructural approach. *PloS one* 8:e65629.

789 LoTurco JJ, Owens DF, Heath MJ, Davis MB, Kriegstein AR (1995) GABA and glutamate
790 depolarize cortical progenitor cells and inhibit DNA synthesis. *Neuron* 15:1287-1298.

791 Love MI, Huber W, Anders S (2014) Moderated estimation of fold change and dispersion for
792 RNA-seq data with DESeq2. *Genome biology* 15:550.

793 Lun MP, Johnson MB, Broadbelt KG, Watanabe M, Kang YJ, Chau KF, Springel MW, Malesz
794 A, Sousa AM, Pletikos M, Adelita T, Calicchio ML, Zhang Y, Holtzman MJ, Lidov HG,
795 Sestan N, Steen H, Monuki ES, Lehtinen MK (2015) Spatially heterogeneous choroid
796 plexus transcriptomes encode positional identity and contribute to regional CSF
797 production. *The Journal of neuroscience : the official journal of the Society for*
798 *Neuroscience* 35:4903-4916.

799 Madan CR (2015) Creating 3D visualizations of MRI data: A brief guide. *F1000Research* 4:466.

800 Madry C, Kyrargyri V, Arancibia-Carcamo IL, Jolivet R, Kohsaka S, Bryan RM, Attwell D
801 (2018) Microglial Ramification, Surveillance, and Interleukin-1beta Release Are
802 Regulated by the Two-Pore Domain K(+) Channel THIK-1. *Neuron* 97:299-312 e296.

803 Milhorat TH, Mosher MB, Hammock MK, Murphy CF (1970) Evidence for choroid-plexus
804 absorption in hydrocephalus. *The New England journal of medicine* 283:286-289.

805 Munk AS, Wang W, Bechet NB, Eltanahy AM, Cheng AX, Sigurdsson B, Benraiss A, Mae MA,
806 Kress BT, Kelley DH, Betsholtz C, Mollgard K, Meissner A, Nedergaard M, Lundgaard I
807 (2019) PDGF-B Is Required for Development of the Glymphatic System. *Cell reports*
808 26:2955-2969 e2953.

809 Netsky MG, Shuangshoti S (1975) The choroid plexus in health and disease. Charlottesville:
810 University Press of Virginia.

811 Oreskovic D, Rados M, Klarica M (2017) Role of choroid plexus in cerebrospinal fluid
812 hydrodynamics. *Neuroscience* 354:69-87.

813 Owens DF, Liu X, Kriegstein AR (1999) Changing properties of GABA(A) receptor-mediated
814 signaling during early neocortical development. *Journal of neurophysiology* 82:570-583.

815 Pisella LI, Gaiarsa J-L, Diabira D, Zhang J, Khalilov I, Duan J, Kahle KT, Medina I (2019)
816 Impaired regulation of KCC2 phosphorylation leads to neuronal network dysfunction and
817 neurodevelopmental pathology. *Science Signaling* 12:eaay0300.

818 Rasmussen R, O'Donnell J, Ding F, Nedergaard M (2020) Interstitial ions: A key regulator of
819 state-dependent neural activity? *Progress in neurobiology* 193:101802.

820 Razzaque MS (2008) Klotho and Na+,K+-ATPase activity: solving the calcium metabolism
821 dilemma? *Nephrology, dialysis, transplantation : official publication of the European*
822 *Dialysis and Transplant Association - European Renal Association* 23:459-461.

823 Saunders NR, Dziegielewska KM, Møllgård K, Habgood MD (2018) Physiology and molecular
824 biology of barrier mechanisms in the fetal and neonatal brain. *The Journal of physiology*
825 596:5723-5756.

826 Schafer DP, Lehrman EK, Kautzman AG, Koyama R, Mardinly AR, Yamasaki R, Ransohoff
827 RM, Greenberg ME, Barres BA, Stevens B (2012) Microglia sculpt postnatal neural
828 circuits in an activity and complement-dependent manner. *Neuron* 74:691-705.

829 Schindelin J, Arganda-Carreras I, Frise E, Kaynig V, Longair M, Pietzsch T, Preibisch S,
830 Rueden C, Saalfeld S, Schmid B, Tinevez JY, White DJ, Hartenstein V, Eliceiri K,
831 Tomancak P, Cardona A (2012) Fiji: an open-source platform for biological-image
832 analysis. *Nature methods* 9:676-682.

833 Schneider CA, Rasband WS, Eliceiri KW (2012) NIH Image to ImageJ: 25 years of image
834 analysis. *Nature methods* 9:671-675.

835 Schuler MH, Lewandowska A, Caprio GD, Skillern W, Upadhyayula S, Kirchhausen T, Shaw
836 JM, Cunniff B (2017) Miro1-mediated mitochondrial positioning shapes intracellular
837 energy gradients required for cell migration. *Molecular biology of the cell* 28:2159-2169.

838 Shaolin Z, Zhanxiang W, Hao X, Feifei Z, Caiquan H, Donghan C, Jianfeng B, Feng L,
839 Shanghang S (2015) Hydrocephalus induced via intraventricular kaolin injection in adult
840 rats. *Folia neuropathologica* 53:60-68.

841 Shen MD, Kim SH, McKinstry RC, Gu H, Hazlett HC, Nordahl CW, Emerson RW, Shaw D,
842 Elison JT, Swanson MR, Fonov VS, Gerig G, Dager SR, Botteron KN, Paterson S,
843 Schultz RT, Evans AC, Estes AM, Zwaigenbaum L, Styner MA, Amaral DG, Piven J,
844 Hazlett HC, Chappell C, Dager S, Estes A, Shaw D, Botteron K, McKinstry R,
845 Constantino J, Pruett J, Schultz R, Zwaigenbaum L, Elison J, Evans AC, Collins DL,

Pike GB, Fonov V, Kostopoulos P, Das S, Gerig G, Styner M, Gu H, Piven J, Infant Brain Imaging Study N (2017) Increased Extra-axial Cerebrospinal Fluid in High-Risk Infants Who Later Develop Autism. *Biological psychiatry* 82:186-193.

Smith GM, Gallo G (2018) The role of mitochondria in axon development and regeneration. *Developmental neurobiology* 78:221-237.

Somasekharan S, Monette MY, Forbush B (2013) Functional expression of human NKCC1 from a synthetic cassette-based cDNA: introduction of extracellular epitope tags and removal of cysteines. *PloS one* 8:e82060.

Sonnhammer ELL, Heijne Gv, Krogh A (1998) A hidden Markov model for predicting transmembrane helices in protein sequences. In: In Proc of Sixth Int Conf on Intelligent Systems for Molecular Biology (Glasgow, J. et al., eds), pp 175-182 Menlo Park, CA: AAAI Press.

Sopjani M, Alesutan I, Dermaku-Sopjani M, Gu S, Zelenak C, Munoz C, Velic A, Foller M, Rosenblatt KP, Kuro-o M, Lang F (2011) Regulation of the Na+/K+ ATPase by Klotho. *FEBS letters* 585:1759-1764.

Spassky N, Merkle FT, Flames N, Tramontin AD, Garcia-Verdugo JM, Alvarez-Buylla A (2005) Adult ependymal cells are postmitotic and are derived from radial glial cells during embryogenesis. *The Journal of neuroscience : the official journal of the Society for Neuroscience* 25:10-18.

Steen RG, Mull C, McClure R, Hamer RM, Lieberman JA (2006) Brain volume in first-episode schizophrenia: systematic review and meta-analysis of magnetic resonance imaging studies. *The British journal of psychiatry : the journal of mental science* 188:510-518.

Steffensen AB, Oernbo EK, Stoica A, Gerkau NJ, Barbuskaite D, Tritsaris K, Rose CR, MacAulay N (2018) Cotransporter-mediated water transport underlying cerebrospinal fluid formation. *Nature communications* 9:2167.

Trapnell C, Williams BA, Pertea G, Mortazavi A, Kwan G, van Baren MJ, Salzberg SL, Wold BJ, Pachter L (2010) Transcript assembly and quantification by RNA-Seq reveals unannotated transcripts and isoform switching during cell differentiation. *Nature biotechnology* 28:511-515.

Vinchon M, Rekate H, Kulkarni AV (2012) Pediatric hydrocephalus outcomes: a review. *Fluids and barriers of the CNS* 9:18.

Vinje V, Eklund A, Mardal KA, Rognes ME, Stoverud KH (2020) Intracranial pressure elevation alters CSF clearance pathways. *Fluids and barriers of the CNS* 17:29.

Volpe JJ (2008) Neurology of the newborn. Philadelphia: Saunders/Elsevier.

Watanabe M, Zhang J, Mansuri MS, Duan J, Karimy JK, Delpire E, Alper SL, Lifton RP, Fukuda A, Kahle KT (2019) Developmentally regulated KCC2 phosphorylation is essential for dynamic GABA-mediated inhibition and survival. *Science Signaling* 12:eaaw9315.

Weiss K, Lazar HP, Kurolap A, Martinez AF, Paperna T, Cohen L, Smeland MF, Whalen S, Heide S, Keren B, Terhal P, Irving M, Takaku M, Roberts JD, Petrovich RM, Schrier Vergano SA, Kenney A, Hove H, DeChene E, Quinonez SC, Colin E, Ziegler A, Rumple

887 M, Jain M, Monteil D, Roeder ER, Nugent K, van Haeringen A, Gambello M, Santani A,
888 Medne L, Krock B, Skraban CM, Zackai EH, Dubbs HA, Smol T, Ghoumid J, Parker MJ,
889 Wright M, Turnpenny P, Clayton-Smith J, Metcalfe K, Kurumizaka H, Gelb BD, Baris
890 Feldman H, Campeau PM, Muenke M, Wade PA, Lachlan K (2020) The CHD4-related
891 syndrome: a comprehensive investigation of the clinical spectrum, genotype-phenotype
892 correlations, and molecular basis. *Genetics in medicine : official journal of the American*
893 *College of Medical Genetics* 22:389-397.

894 Williams CJ, Naito T, Arco PG, Seavitt JR, Cashman SM, De Souza B, Qi X, Keables P, Von
895 Andrian UH, Georgopoulos K (2004) The chromatin remodeler Mi-2beta is required for
896 CD4 expression and T cell development. *Immunity* 20:719-733.

897 Zeuthen T (1994) Cotransport of K+, Cl- and H2O by membrane proteins from choroid plexus
898 epithelium of Necturus maculosus. *The Journal of physiology* 478 (Pt 2):203-219.

899 Zeuthen T, Macaulay N (2012) Cotransport of water by Na(+)-K(+)-2Cl(-) cotransporters
900 expressed in Xenopus oocytes: NKCC1 versus NKCC2. *The Journal of physiology*
901 590:1139-1154.

902 Zhang Y, Huang G, Shornick LP, Roswit WT, Shipley JM, Brody SL, Holtzman MJ (2007) A
903 transgenic FOXJ1-Cre system for gene inactivation in ciliated epithelial cells. *American*
904 *journal of respiratory cell and molecular biology* 36:515-519.

905

Figure 1

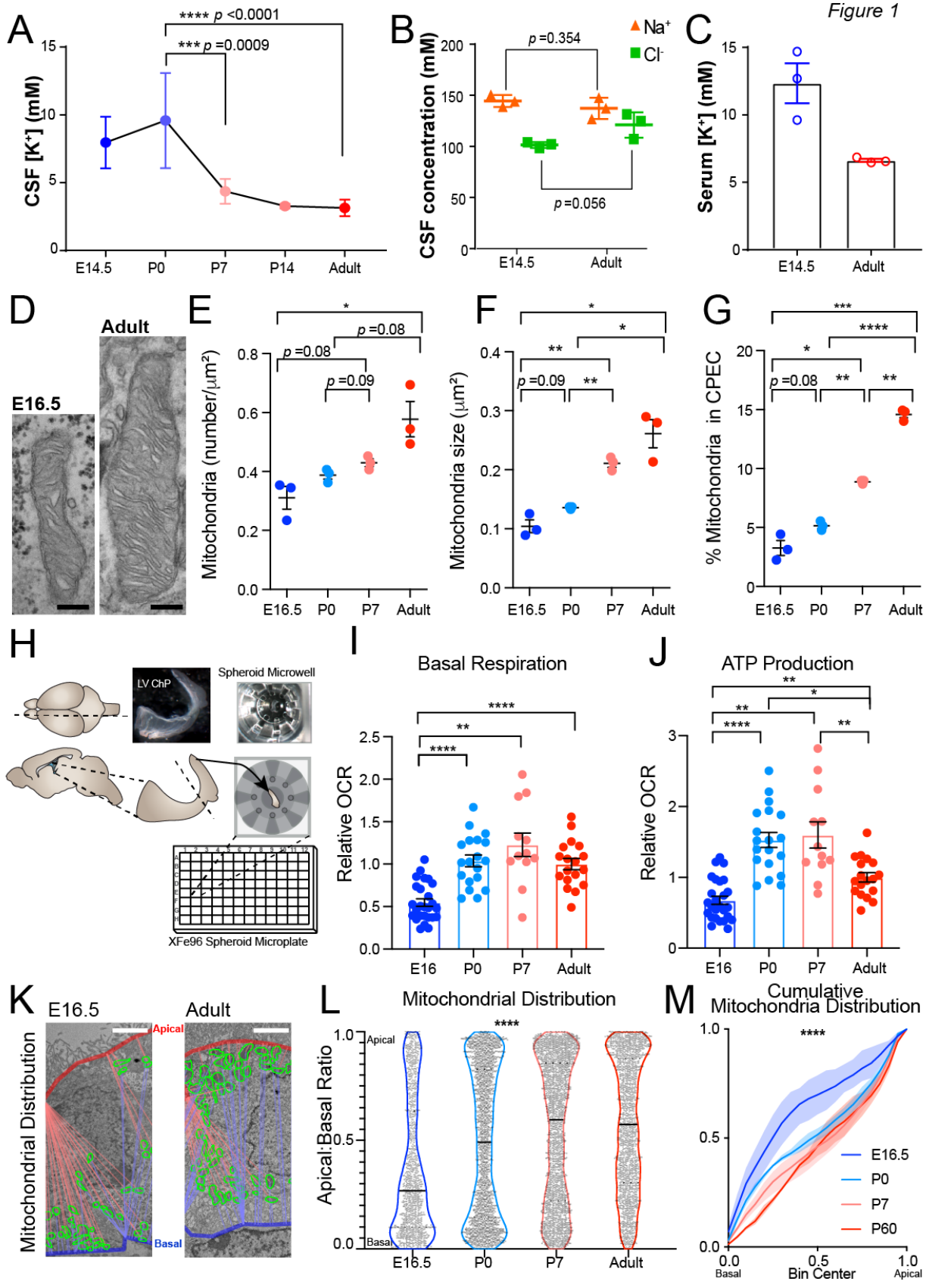

907 **Fig. 1. Postnatal CSF [K^+] decrease coincides with increased ChP metabolism. (A)** ICP-OES
908 quantification of CSF [K^+]. N = 6, **** $p < 0.0001$ by one-way ANOVA. Sidak's test was used
909 for P0 vs. P7 and P0 vs. adult comparison. *** $p = 0.0009$, **** $p < 0.0001$. **(B)** ICP-OES and
910 IC measurements of E14.5 and adult mouse CSF [Na^+] and [Cl^-]. N=3; Welch's t-test. **(C)** ICP-
911 OES measurements of embryo vs. adult mouse serum [K^+]. N=3. **(D)** Transmission micrographs
912 of mitochondria in LVChP. (**E-G)** Quantification of mitochondrial number (**E**), area (**F**), and %
913 area occupancy (**G**) in ChP epithelial cells. N =3 animals, 5-10 FOV per animal, *$p < 0.05$, **p
914 < 0.01, ***$p < 0.005$, ****$p < 0.001$; Welch's t-test. **(H)** Schematic of explant-based Agilent
915 Seahorse XFe96 test. (**I-J)** Oxidative respiration metrics over development. *$p < 0.05$, **$p <$
916 0.01, ****$p < 0.0001$; Welch's ANOVA with Dunnett's T3 multiple comparison test. **(K-L)**
917 Mitochondrial distribution between the apical and basal surfaces (Apical: Basal proximity ratio).
918 1 = apical surface. 0 = basal surface. Solid line indicates median and dashed line indicates
919 upper/lower quartiles. **** $p < 0.0001$; Kolmogorov–Smirnov test. **(M)** Cumulative distribution
920 of mitochondrial localization. Solid lines are the mean, shaded area represents the range. Scale
921 bar (d) = 250nm, (k) = 2µm. Unless otherwise noted, all quantitative data are presented as Mean
922 ± SEM.
923

Figure 2

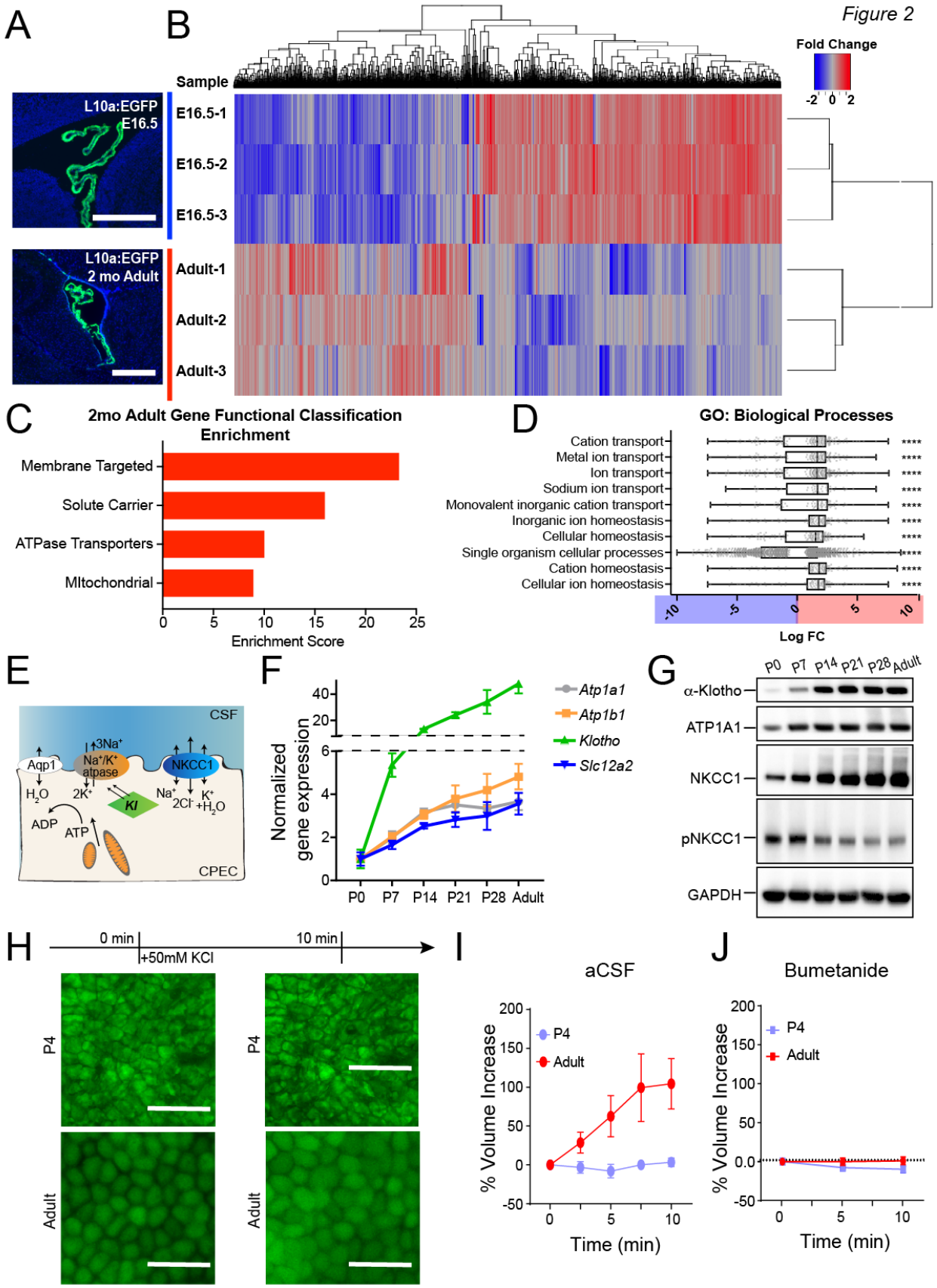

925 **Fig. 2. Choroid plexus epithelial cells display age-dependent translation of ion and water**
926 **transporters, in particular NKCC1. (A)** Rpl10a-conjugated EGFP expression in ChP epithelial
927 cells after *Foxj1*-Cre recombination in TRAP-BAC mice. **(B)** Heatmap and hierarchical
928 clustering of differentially expressed genes (adjusted $p < 0.05$). **(C)** Top 4 gene functional
929 clusters shown by DAVID to be enriched in Adult ChP epithelial cells over E16.5 ChP epithelial
930 cells. **(D)** Top 10 significantly enriched gene ontology (GO) terms for "Biological processes".
931 Plotted with boxes for quartiles and whiskers for 5th and 95th percentiles. The $\log_{10}$ fold change
932 (LogFC) is plotted for each expressed gene for the network. Positive values (red) indicate Adult
933 enrichment and negative values (blue) indicate E16.5 enrichment. *p* values are corrected for
934 multiple measures using Bonferroni correction. $^{**}p \leq 0.01$, $^{***}p \leq 0.001$, $^{****}p \leq 0.0001$. **(E)**
935 Schematics demonstrating the interaction of NKCC1, Na^+/K^+-ATPase, and Klotho on the apical
936 membrane of a ChP epithelial cell (CPEC). **(F-G)** RT-qPCR and immunoblotting of LVChP
937 during postnatal development. **(H)** Fluorescence images of Calcein-AM labeled epithelial cells
938 from LVChP explants under high extracellular K^+ challenge. Scale bar = 50µm. **(I-J)**
939 Quantification of ChP epithelia cellular volume by IMARIS 3D analysis. Percent volume
940 increase = dV/V_0 for each timepoint (t). V_0 = initial volume of the cell; t = subsequent timepoint
941 after addition of challenge; $dV = V_t - V_0 \times 100\%$. At least 10 cells were analyzed for each explant
942 from one animal; N = 4.

Figure 3

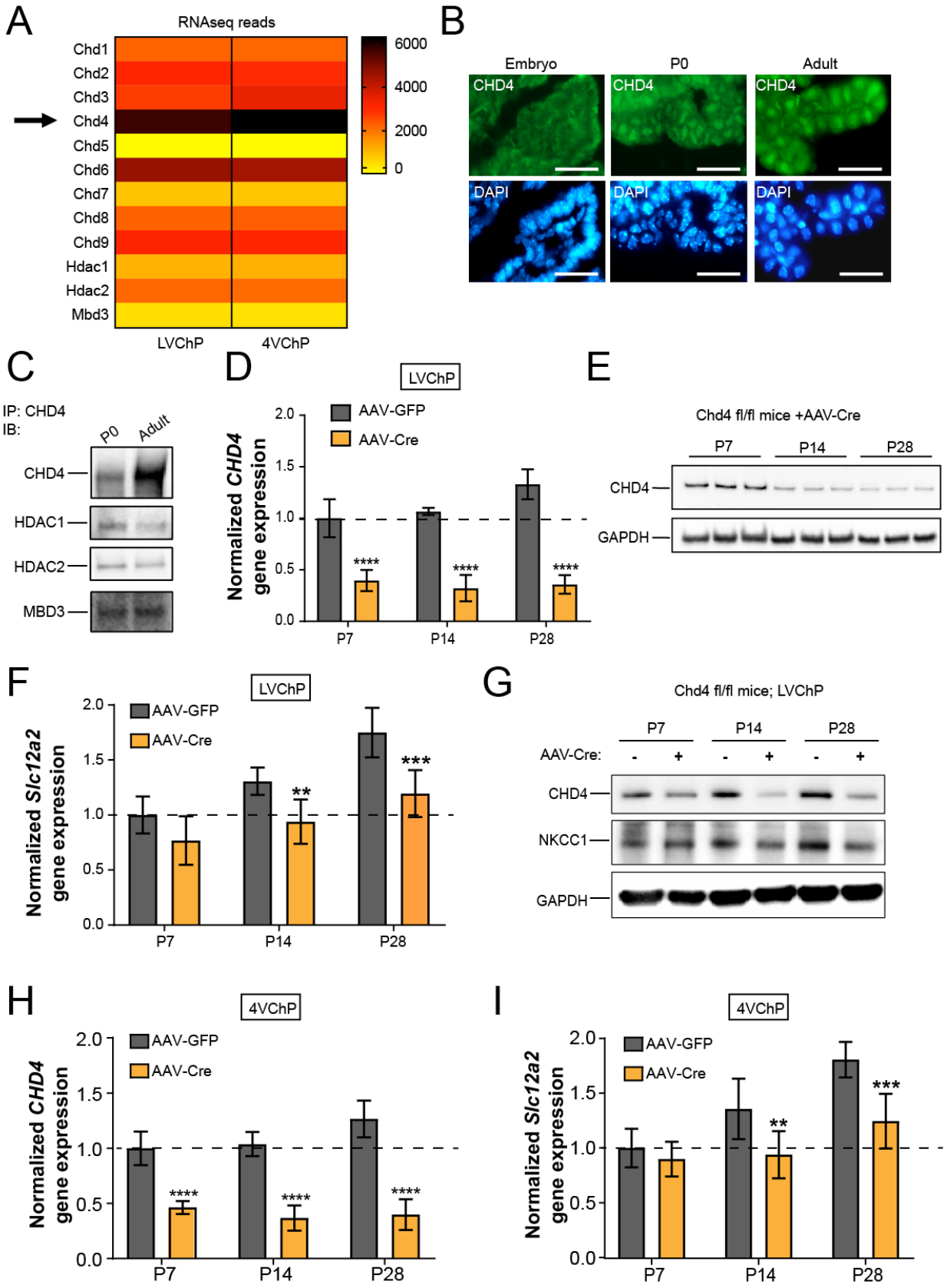

Fig. 3. NKCC1 temporal expression requires CHD4/NuRD complex. (A) RNAseq data showing expression of CHD and other NuRD units by the ChP. **(B)** Immunofluorescence images of CHD4 in the ChP epithelia at E16.5, P0, and adult; Scale bar = 30μm. **(C)** Immunoblots of Co-IP by CHD4 antibody. **(D)** RT-qPCR of CHD4 transcripts in ChP with AAV2/5-Cre infection.**** $p< 0.0001$, N = 7, Welch's t-test. **(E)** Immunoblot of CHD4 in AAV-cre mice ChP lysate with. **(F)** RT-qPCR of NKCC1 expression in AAV-cre vs. AAV-GFP mice ChP. All values were normalized to P7 AAV-GFP control mice. **$p = 0.0015$, ***$p < 0.001$, N = 7, Welch's t-test. **(G)** Immunoblot of NKCC1 in LVChP lysates from AAV-cre vs. AAV-GFP mice. **(H-I)** CHD4 and NKCC1 RT-qPCR in 4VChP. ** p = 0.0083, *** $p < 0.001$, **** $p < 0.0001$, N = 7, Welch's t-test.

Figure 4

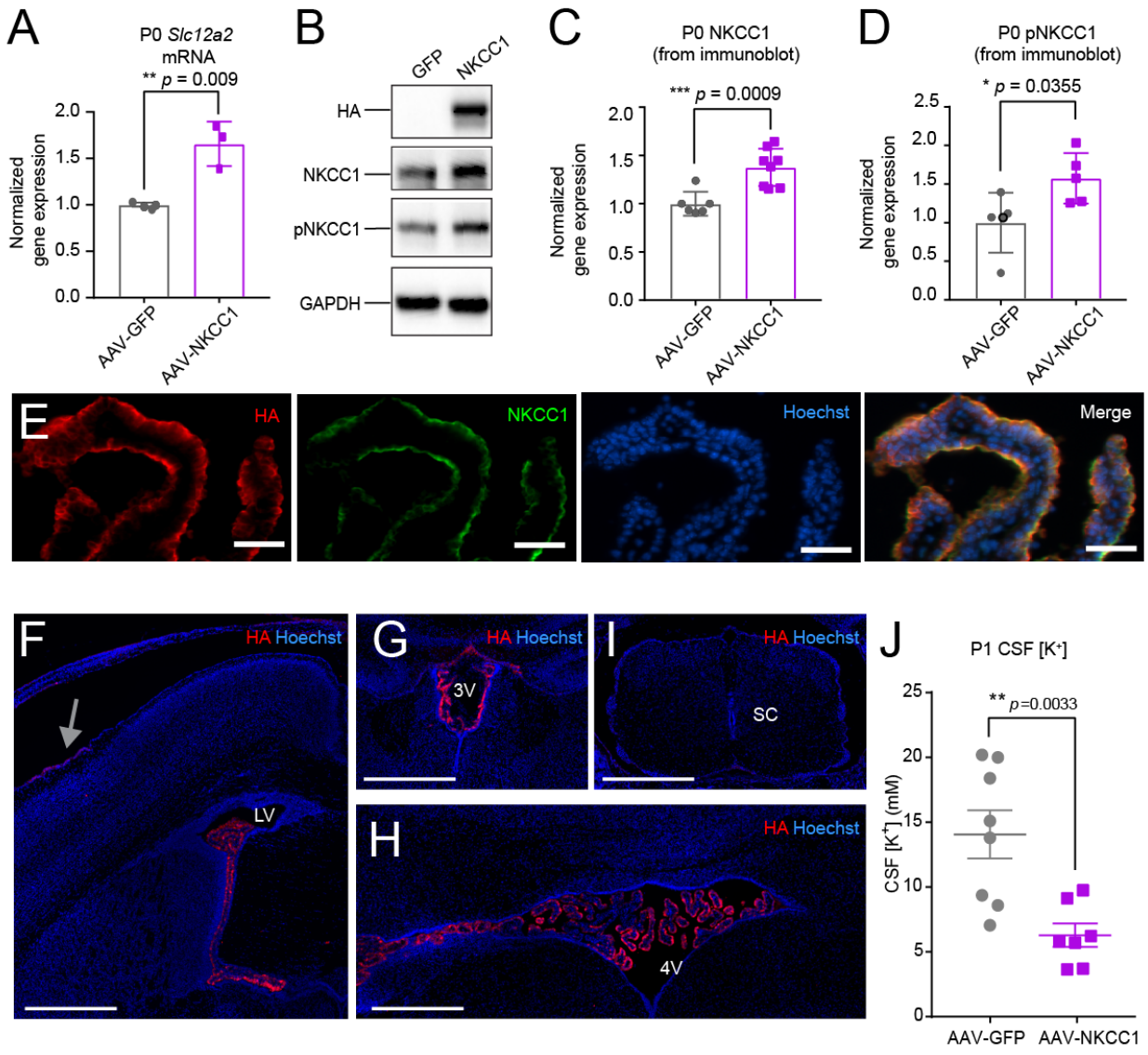

Fig. 4. ChP NKCC1 actively mediates CSF K^+ clearance in the first postnatal week. (A) RT-qPCR of NKCC1 mRNA levels in P0 mice. ** $p = 0.009$, N=3; Welch's t-test. **(B)** Immunoblots from AAV-NKCC1 vs. AAV-GFP P0 mice ChP lysates. **(C-D)** Quantification of all immunoblots of NKCC1 (**C**) *** $p = 0.0009$, N=7; Welch's t-test; and pNKCC1 (**D**) * $p = 0.0355$, N=5; Welch's t-test. **(E)** Immunofluorescence images showing co-localization of 3xHA tag and NKCC1 in P0 ChP. Scale bar = 50µm. **(F-I)** Immunofluorescence images of HA in AAV2/5-NKCC1 transduced brain at P1: the LVChP (**F**), 3rd ventricle ChP (3VChP; **G**), 4VChP (**H**), and the spinal cord (**I**; sc = spinal cord). Traces of HA is shown in the meninges near the injection site (grey arrow). Scale bar = 500µm. **(J)** ICP-OES measurements of CSF [K^+] from AAV-NKCC1 vs. AAV-GFP P1 mice (N = 8 in AAV-GFP cohort; N = 7 in AAV-NKCC1 cohort). **$p = 0.0033$; Welch' t-test.

Figure 5

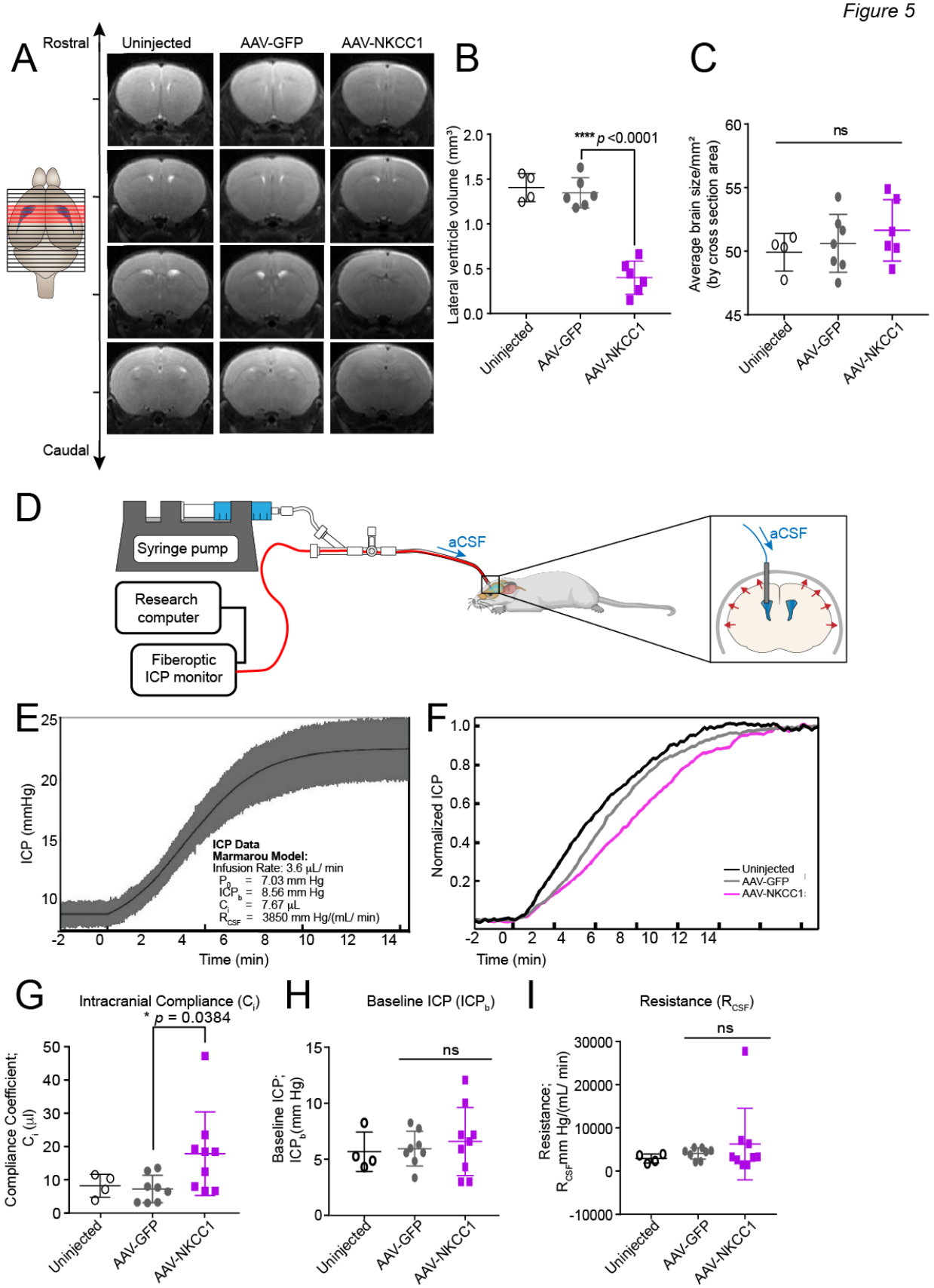

971 **Fig. 5. ChP NKCC1 overexpression reduces brain ventricular volume and increases**
972 **intracranial compliance. (A)** T2-weighted live MRI images. Only slices with visible LV are
973 shown (marked red in the schematics). **(B)** LV volumes. Uninjected N = 4; AAV-GFP and AAV-
974 NKCC1 N = 6; ****$p < 0.0001$; Welch's t-test. **(C)** Brain sizes, which are presented as the
975 average coronal section area from all images with visible ventricles (NKCC1 OE data were
976 calculated using the matching images to the controls, regardless of ventricles visibility).
977 Uninjected N = 4; AAV-GFP and AAV-NKCC1 N = 6; Welch's t-test. **(D)** Schematic of *in vivo*
978 constant rate CSF infusion test. **(E)** Example of ICP curve during the infusion test (infusion
979 begins at 0 min) in an AAV-GFP mouse, fitted to Marmarou's model. Values extracted include:
980 baseline ICP (ICP_b), a pressure-independent compliance coefficient (C_i) and the resistance to
981 CSF outflow (R_{CSF}). **(F)** Example ICP recordings from AAV-NKCC1 mice and controls. For
982 clarity, data have been low pass filtered to remove the waveform components. **(G)** Compliance
983 coefficients. Uninjected N = 4; AAV-GFP N = 8; AAV-NKCC1 N = 9; *$p = 0.0384$; Welch's t-
984 test. **(H-I)** Plots of baseline ICP and resistance to CSF outflow (R_{CSF}) at 5-7 weeks. Uninjected
985 N=4, AAV-GFP N=8, AAV-NKCC1 N=9; Welch's t-test.
986

Figure 6

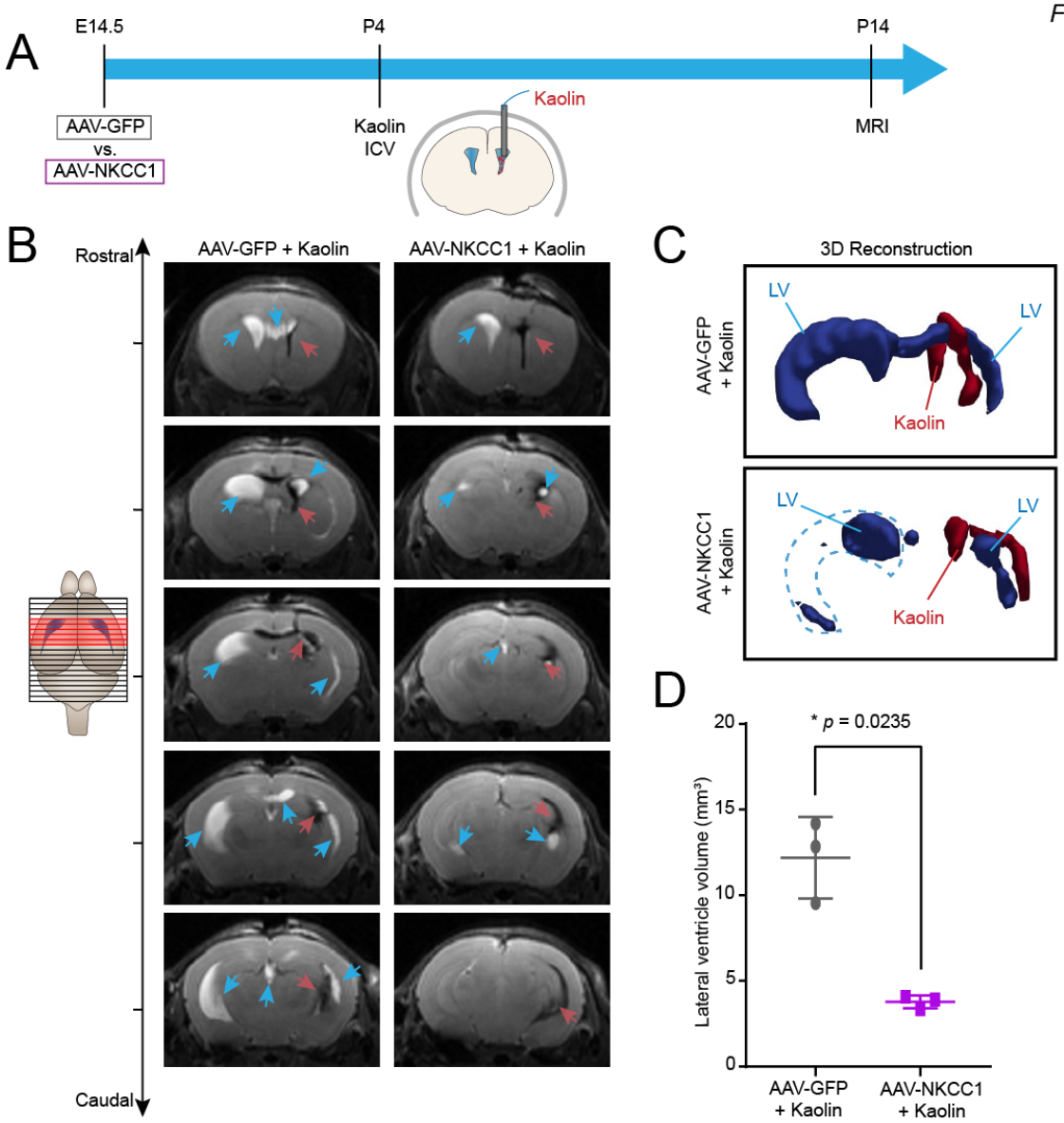

Fig. 6. ChP NKCC1 overexpression mitigates ventriculomegaly in an obstructive hydrocephalus model. (A) Schematics showing the workflow: E14.5 in utero ICV of AAV2/5-NKCC1 or AAV2/5-GFP, followed by ICV of kaolin at P4, and MRI at P14. **(B)** Representative sequential brain images (rostral to caudal) by T2-weighted live MRI images. Blue arrows: LV. Red arrows: kaolin. **(C)** 3D reconstruction of the LV and kaolin deposition. LV: blue. Kaolin: red. **(D)** LV volumes. N = 3; $*p = 0.0.0235$; Welch's t-test.

Figure 7

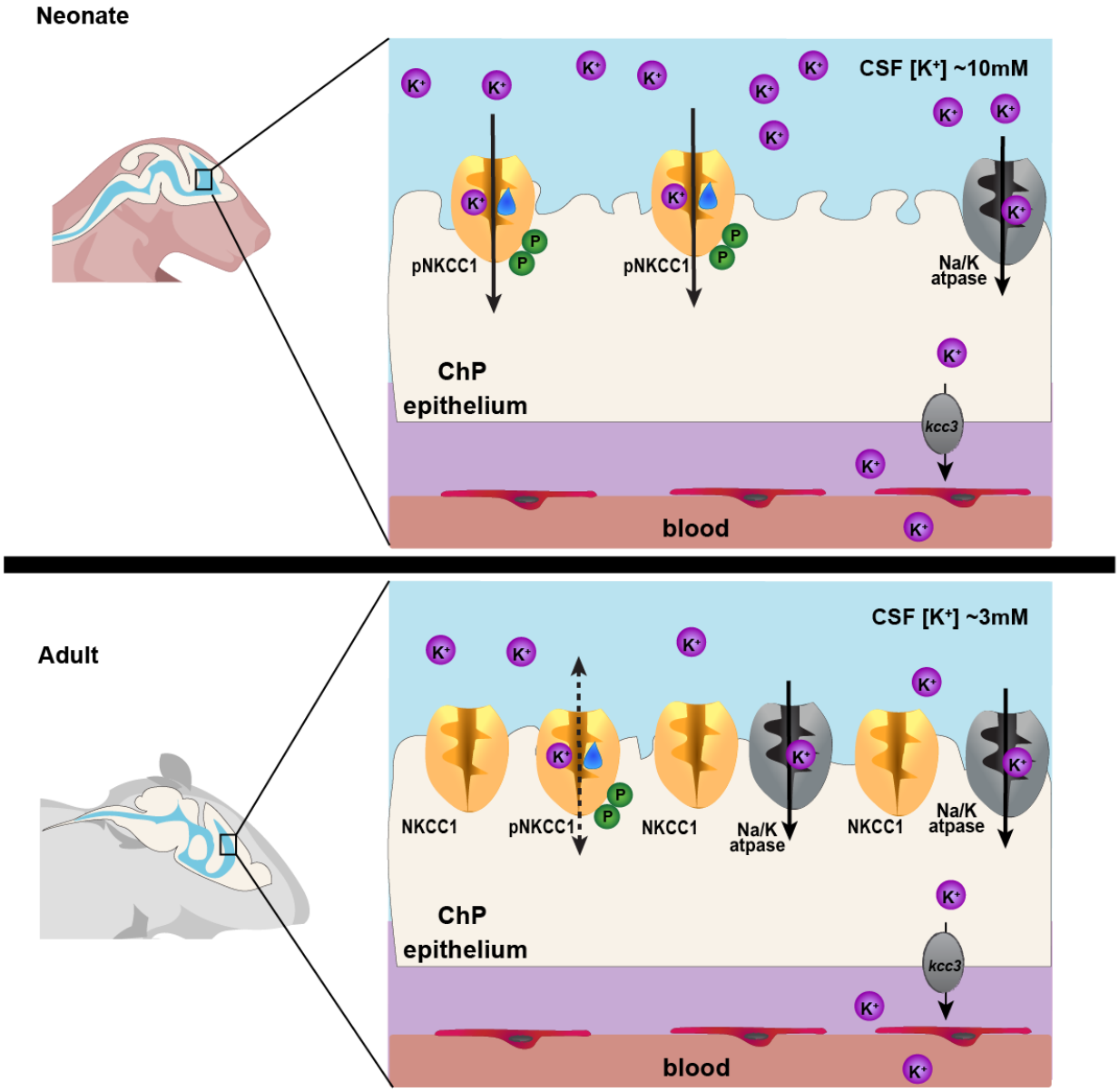

995 **Fig. 7. Working model of ChP NKCC1 mediating K^+-driven CSF outflow.** The schematics
996 describes ChP NKCC1 mediated K^+ and water clearance from CSF in neonatal mice, in
997 comparison to the adult scenario. For simplicity and clarity, only K^+ is depicted among all ions
998 and only NKCC1 and Na^+/K^+-ATPase are included. Neonatal (P0-7, left) ChP has high pNKCC1
999 than adult, albeit lower total NKCC1. Neonate CSF [K^+] is 2-3 fold higher than adult. With
1000 similar [Na^+] and [Cl^-], this [K^+] difference is sufficient to alter the total Nernst potential of
1001 epithelial cells and bias NKCC1 transport of K^+, together with water, out of CSF into the ChP in
1002 neonates.
1003